THERMAL RADIATION FROM MODULATED METAL SURFACES

by

SAIFA AMIN

Submitted to the Graduate School of Engineering and Natural Sciences
in partial fulfilment of
the requirements for the degree of
Master of Science

Sabancı University

July 2023

ABSTRACT

THERMAL RADIATION FROM MODULATED METAL SURFACES

SAIFA AMIN

Physics, M.Sc. Thesis, July 2023

Thesis Supervisor: Prof. Dr. İsmet İnönü Kaya

Keywords: Graphene, Chemical Vapor Deposition (CVD), Three Dimensional
Periodically Patterns Surfaces, Thermal Radiation

In this thesis we developed techniques to fabricate various periodically or quasi periodically corrugated graphene and metal films on PDMS. Period of the films could be repetitively modulated by mechanically induced strain. We analyzed the emissivity of the surfaces in infrared range and the effect of mechanical strain towards developing emissivity control mechanisms. Such surfaces are expected to create enhancement or diminution in the emissivity at wavelengths related to the corrugation periodicity. We applied multiple approaches to create modulable thin films. A soft fluoropolymer (CFx) skin layer with controllable thickness was deposited on PDMS by CHF_3 plasma gas. Pitch sizes were controlled by varying the tensile strain of the PDMS substrate and RIE treatment time. However, graphene did not transfer on CFx with full surface coverage. A uniform 3D modulation of graphene on PDMS was achieved via mold fabricated by lithography and directional wet etching. Multilayer graphene films were synthesized on a patterned nickel film using chemical vapor deposition and transferred on to PDMS while maintaining the structural integrity of graphene. Consequently, a crack-free uniform multilayer graphene on PDMS with controlled periodicity such as the wavelength, orientation, and spatial location has been achieved. Ni stripes on $SiO2$ deposited lift off with various periodicity and aspect ratio showed modulation in IR emissivity. Using another technique spontaneously corrugated Ni thin film on top of PDMS with different periodicity were also synthesized. These patterned metal surfaces exhibited tunable emissivity in the IR wavelengths correlated with the corrugation periodicity of the films.

ÖZET

MODÜLE METAL YÜZEYLERDEN TERMAL RADYASYON

SAIFA AMIN

Fizik, Yüksek Lisans Tezi, Temmuz 2023

Tez Danışmanı: Prof. Dr. İsmet İnönü Kaya

Anahtar Kelimeler: Grafen, Kimyasal Buhar Biriktirme (CVD), Üç Boyutlu Perioyodik Desenli Yüzeyler, Termal Radyasyon

Bu tezde, PDMS üzerinde çeşitli periyodik veya yarı periyodik oluklu grafen ve metal filmler imal etmek için teknikler geliştirdik. Filmlerin periyodu, mekanik olarak indüklenen gerilme ile tekrar tekrar modüle edilebilir. Kızılötesi aralıktaki yüzeylerin yayılımını ve mekanik zorlamanın yayma kontrol mekanizmaları geliştirmeye yönelik etkisini analiz ettik. Bu tür yüzeylerin, dalgalanma periyodikliği ile ilgili dalga boylarında emisyonda artış veya azalma oluşturması beklenir. Modüle edilebilir ince filmler oluşturmak için birden fazla yaklaşım uyguladık. Kontrol edilebilir kalınlığa sahip bir yumuşak floropolimer (CFx) tabakası, CHF3 plazma gazı ile PDMS üzerinde biriktirildi. Oluk adım boyutu, PDMS substratının gerilme gerilimi ve RIE süresi değiştirilerek kontrol edildi. Bununla birlikte, grafen, tam yüzey kaplamasıyla CFx üzerinde transfer olmadı. PDMS üzerinde tekdüze bir 3B grafen modülasyonu, litografi ve yönlü ıslak aşındırma ile üretilen kalıp yoluyla elde edildi. Çok katmanlı grafen filmler, kimyasal buhar biriktirme kullanılarak desenli bir nikel film üzerinde sentezlendi ve grafenin yapısal bütünlüğü korunurken PDMS'ye aktarıldı. Sonuç olarak, dalga boyu, oryantasyon ve uzamsal konum gibi kontrollü periyodikliğe sahip PDMS üzerinde çatlaksız tek tip çok katmanlı bir grafen elde edilmiştir. SiO2 biriken Ni şeritleri, çeşitli periyodiklik ve en-boy oranıyla, IR emisyonunda modülasyon gösterdi. Başka bir teknik kullanılarak, farklı periyodikliğe sahip PDMS'nin üstünde kendiliğinden oluklu Ni ince filmler de sentezlendi. Bu desenli metal yüzeyler, filmlerin oluklanma periyodu ile ilişkili olarak IR dalga boylarında ayarlanabilir emisyon sergilemiştir.

ACKNOWLEDGEMENTS

First, I would like to thank Prof. Dr. İsmet İnönü Kaya, my advisor for his unwavering encouragement, knowledge, and support during my M.Sc. studies and research. I want to express my gratitude to him for all the of the opportunity he has given me to do my research.

I would like to thank Assoc. Prof. Dr. Emre Erdem and Prof. Dr. Engin Tıraş for devoting valuable time to my thesis committee.

In addition, I would like to thank the members of Sabanci University Nanotechnology Research and Application Center, and Faculty of Engineering and Natural Sciences of Sabanci University for providing facilities to carry out the research work. The experimental research done in this thesis is partly funded by FNSS.

My sincere thanks to Dr. Hadi Khaksaran and Süleyman Çelik for sharing their valuable experience and worthy guidance. My heartfelt thanks to Ege Aygit, Maryam Sepehri Gohar, Tuna Alp, Ara Rahimpour, Pouya Sharbati, Elham Ghorani, Solomon Brhanu Samuel, Ndiogou Niang, and Bilal Cantürk for their whole-hearted friendships.

Most importantly, I am truly grateful to my family for their immense love and persistent support. I will not be able to achieve my academic goals without their encouragement, self-devotion, and support.

TABLE OF CONTENTS

LIST OF TABLES

LIST OF FIGURES

LIST OF ABBREVIATIONS

ε	:	emissivity
IR	:	Infrared
2D	:	two-dimensional
FTIR	:	Fourier transform infrared spectrometer
3D	:	three-dimensional
T	:	transmittance
EBL	:	electron beam lithography
PECVD	:	Plasma enchaced chemical vapor deposition
CVD	:	Chemical Vapor Deposition
PDMS	:	Polydimethylsiloxane
UVO	:	ultraviolet-ozone
SA	:	stretching apparatus
E	:	tensile strain
BOE	:	buffered oxide etch
RIE	:	reactive ion etching
$(NH_4)_2S_2O_8$	:	ammonium persulfate
SEM	:	Scanning Electron Microscopy
PMMA	:	Polymethyl Mathacrylate
PS	:	Polystryrene
CF_x	:	fluoropolymer
AFM	:	atomic force microscopy
HOPG	:	Highly Oriented Pyrolytic Graphite
IPA	:	Isopropyl Alcohol
DI	:	Deionized
SiO_2	:	Silicon Dioxide

μm	: Micrometer
nm	: Nanometer
cm	: Centimeter
Cu	: Copper
H	: Hydrogen
C	: Carbon
Ar	: Argon
CH_4	: Methane
Gr	: Graphene
O_2	: Oxygen

1. INTRODUCTION

All objects emit electromagnetic radiation at finite temperatures, this is known as blackbody radiation. The amount of thermal energy emitted from a heated surface per unit area is described by $P = \varepsilon\sigma T^4$ called Stefan-Boltzmann law, where $\varepsilon(\lambda,T)$ represents surface emissivity, T temperature of the surface and σ the Stefan-Boltzmann constant. Emissivity is a function of temperature and wavelength. Surface composition, including material, surface thickness, and surface morphology, determines the variation of surface emissivity with respect to wavelength.

All objects radiate thermal energy, although some wavelengths in the electromagnetic spectrum are invisible. The hotter object emits more power with a peak at shorter wavelengths given by Wien's Law. The term "heat signature" refers to the radiation's spectrum. When two objects with subtly different heat signatures are placed next to each other, a thermal sensor can easily detect them. As a result, completely dark surroundings are visible to thermal cameras. For example, the human body radiates heat in a way that makes it easy for IR cameras to identify them from their surroundings. Infrared cameras are capable of capturing infrared light and processing the information to create an image via digital or analog video outputs. An infrared camera uses detectors to capture a certain range of invisible wavelengths (0.9–1.7, 2-5 or 7-12 microns). The camera has a great deal of infrared sensors placed in pixels. The radiation emitted from the target area is captured by each pixel, which is then expressed separately in the final image. The full temperature of each pixel, not simply the average, is displayed in the final image. The color map can be chosen and specifically designed to provide a visual representation of the various wavelength emissions. Based on the chosen color map, the combined readings of each pixel are processed to create a thermal image. Most thermal images represent blue for colder temperatures, yellow for medium, and red for hot temperatures. The generated

image is called thermography.
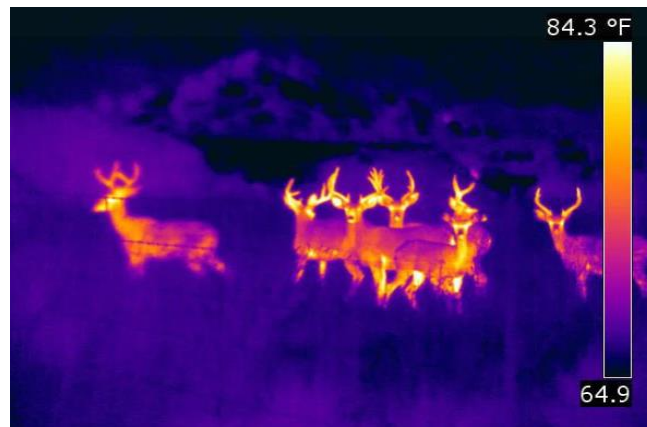
Figure 1: Heat differences with different color palettes detected by IR camera

Target detection is accomplished by comparing the IR emissions from the target and the surrounding background. According to Planck's Law, a black body's IR emission depends on its absolute temperature and frequency. The wavelength, temperature, and gas composition of radiation-participating atmosphere all affect how much IR radiation is attenuated there. The range of the infrared spectrum is from 0.77–1000 μm. Two atmospheric windows with high transmittance, 3 μm to 5 μm and 8 μm to 12 μm, are frequently utilized for tracking and surveillance. Due to the absorption and scattering properties of carbon dioxide and water vapor, there is a considerable attenuation of Infrared outside these windows. [1] The 3–5 μm window is more suitable for locating hot spots since it has a higher peak emission temperature (450 °C). The 8–12 μm band is used for emissions from bigger surfaces at low temperatures since it has a lower peak emission temperature (17 °C). [2]
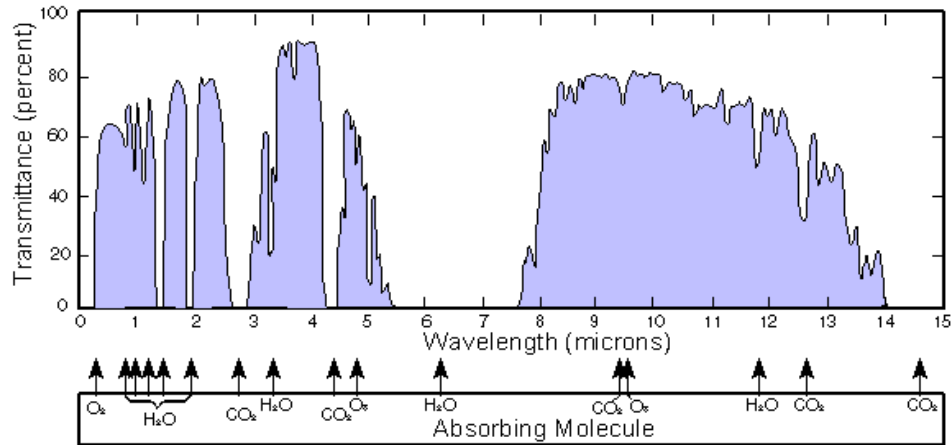
Figure 2: Electromagnetic spectral transmission of air. Atmospheric window resides between 3-5 μm and 8-14μm.

Thermal camouflage requires regulating the thermal radiation spectrum emitted from a surface in such a way that thermal cameras can't differentiate its temperature from the background. Thermal cameras are less effective in warmer environments when everything in the frame is similar in temperature. Camouflage technology is categorized into thermal camouflage and color camouflage. *Color camouflage* can be produced by controlling the transmission or reflection of light so that it to match the appearance of the object to the sorrounding in the visible or near IR region [3-5]. *Thermal camouflage* requires controlling the thermal radiation spectrum emitted from a surface. Thermal camouflage can trick thermal imagers. It can distinguish objects using the difference in radiation temperature between objects and the background.

Thermal camouflage has received a lot of attention due to improvements in IR surveillance technologies. The objective of thermal camouflage is to change a target's actual temperature to blend it with its surroundings temperature.

Recently, there has been an upsurge in interest in finding materials and devices for active thermal camouflage. Two fundamental techniques are used. The first technique centers on *modifying an object's surface emissivity* [6]. Stefan–Boltzmann law states that at low temperatures, black background and a surface of low emissivity have the same emissive power. Low-emissivity films or coatings can thereby reduce the radiation temperature of an object and make it disappear into the background [7-9]. Traditional camouflage

3

coatings can only hide objects against a specific background temperature since they have a fixed emissivity. Once the background temperature has been changed, thermal imagers will be capable of easily finding an object due to a difference in its radiation temperature between it and the background. Thermal camouflage with the *tunable thermal emissivity* of objects can be used at various background temperatures. This strategy is expanded to include tunable surface emissivity, which enables adaptive IR camouflage, or the ability to match the thermal signature with the background in real-time. [6, 9, 10]. A variety of methods have been used to achieve infrared emissivity or reflectivity control, including mechanical actuation of graphene [11] inter-subband transition manipulation of photonic crystal slabs [12] light-excited infrared metamaterial [13] and many more.
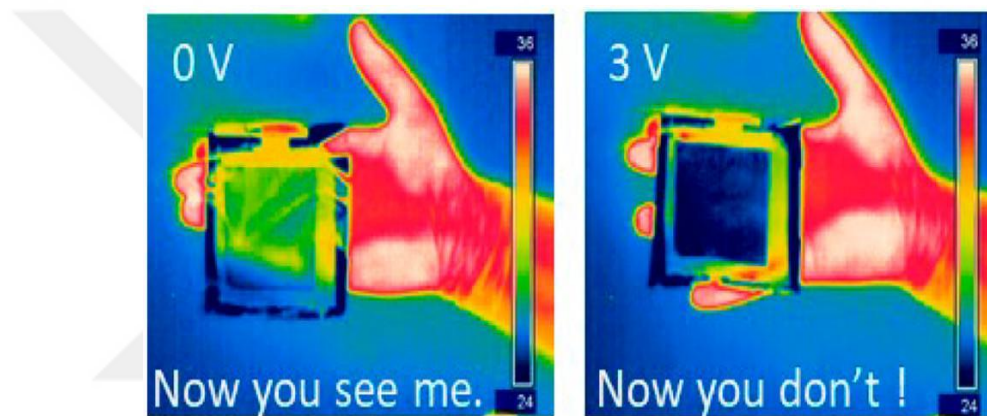
Figure 3: Thermal camera images of the thin, light, and flexible devices, placed in the hand with voltage biases of 0 and 3, cover their surroundings. The device has a electrically controlable transmission across the infrared (IR) spectrum. [9]

Most emissivity and thermal emissivity methods are static [14-30] and support many applications such as thermophotovoltaics [31-37] sensing [38, 39] and radiative cooling [40-43]

A second approach is based on the emergence of *thermal metamaterials or thermotics* [44]. It uses a design to direct thermal conduction and radiation in materials with non-uniform distributions of thermal conductivity or refractive index to create *thermal cloaks*. This thermal metamaterial technique is explored at the fundamental level.

Graphene offers new opportunities to control thermal radiation at infrared wavelengths [3, 6, 9, 11, 45-47] Flat graphene has 2.7% optical absorption in a wide spectrum including UV, visible, and IR (0.1-20 µm). This property can be controlled by altering its morphology [48-56] For example, *a periodically modulated graphene structure modifies the emission spectrum for a range of periodic dimensions over the whole electromagnetic spectrum due to the interference phenomenon* [11]. It has been demonstrated that when the surface of the modulated graphene samples has patterns, its emissivity spectra can be tuned by controlling the pitch size. Increasing pitch sizes moves the high emissivity spectrum towards longer wavelengths. A low pitch size of 140 nm is fabricated on PS shows high emissivity in the UV spectrum from the wavelengths of 0.8 to 300 nm. In contrast, a high pitch size of 10 µm fabricated PDMS, exhibits high emissivity in the mid IR wavelengths (7 and 19 µm) [11].

In this regard, flexible materials, such as polystyrene (PS) and polydimethylsiloxane (PDMS) are utilized to provide morphology-controlled dynamic emissivity variations. Graphene was transferred on a PDMS substrate to attain longer pitch sizes [11]. Crumpled pitch can then be modulated by applying strain which is reversible during cyclical stretching and releasing [57]. At high strain regimes, soft (CF_x) skin layers on stretched PDMS films prevented surface wrinkling from cracking. The soft skin doesn't form secondary structures up to the strain of 60%. Since Young's modulus of the CF_x skin layer is 40-fold lower than that of other hard silica skin layers, it is considered a soft layer and thus resistant to crack formation. A (CF_x) layer with controllable thickness is deposited on PDMS by CHF_3 plasma gas. The skin layer over the substrate doesn't show any cracks up to 25% strain. [53]

2. GROWTH OF GRAPHENE BY CHEMICAL VAPOR DEPOSITION (CVD)

2.1. Introduction

Graphene is a conjugated sp^2 carbon sheet arranged in a 2D hexagonal lattice [58]. Graphene has high mobility, flexibility, and optical transparency [59]. Its structural flexibility is reflected in its electronic properties. Electrons in graphene have a linear relationship between the energy and the momentum, so they act as massless Dirac fermions [60-62]. The electrons in graphene have extremely long mean free pathways and insensitive to disorder and electron-electron interactions. It shows high crystal quality and ballistic transport on a submicron scale. The carriers mimicking photons have a zero mass and constant speed of 10^6 ms^{-1} [59].
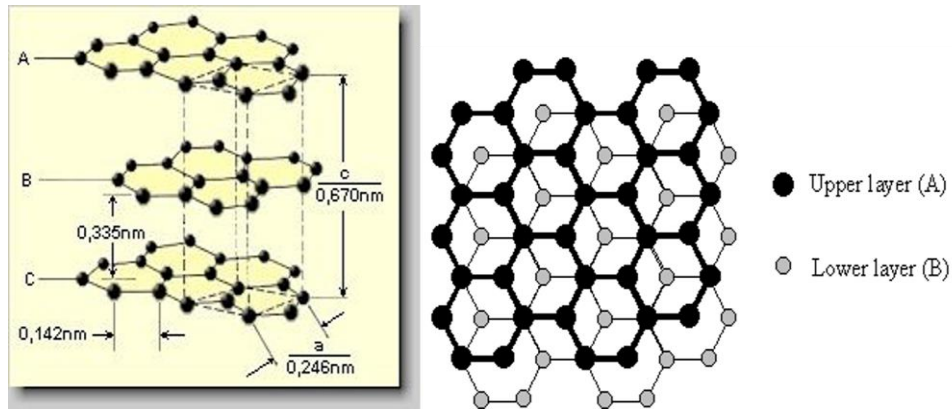
Figure 4: Graphene lattice structure demonstrated as one layer of graphite (top). Electronic dispersion in the honeycomb lattice of graphene (bottom). The energyspectrum is displayed on the left in the eV units, and the energy bands close to one of the Dirac points are zoomed in on the right. [63]

Table 1: Properties of pristine graphene.

	Graphene			
Charge mobility	10.000- 200.000	$cm^2V^{-1}s^{-1}$	100 – 1.500	**Silicon**
Electrical Conductivity	10^6	Ω^{-1}-cm	$6x10^5$	**Silver**
Thermal Conductivity	5.000	$W\text{-}K^{-1}m^{-1}$	400	**Copper**
Young's modulus	1,0	TPa	1,2	**Diamond**

Graphene has exceptional optical properties. Despite being only one atom thick, it can be seen optically [64, 65]. Its transmittance (T) can be expressed as fine-structure constant [66]. Pauli blocking cause saturable absorption [67, 68] and non-equilibrium carriers cause hot luminescence [69-72]. Luminescence can also result from physical and

chemical modifications. [73-76] Thus graphene is a perfect material for photonic and optoelectronic applications.

Graphene, one-atom-thick carbon fabric, combines extraordinary mechanical strength [77], extremely high electrical [78] and thermal conductivities [79], gas impermeability, and many other superior features, making it highly appealing for a variety of applications. [80] like flexible electronics, bio/chemical sensors, optoelectronics, energy generation and storage. [81] With the CVD technique centimeter-scale single crystalline graphene can be synthesized. Metal substrates are required to catalyze the graphene growth in the CVD method. [82-84] For the metals that have high carbon solubility (e.g.: Ni, Fe), carbon species will diffuse into the metal catalyst substrate at high temperature. They segregate and precipitate during the cooling phase, forming graphene sheets. Whereas, for metals that have low carbon solubility (Cu), carbon atoms stay on the metal substrate surface, surface adsorption. [85]
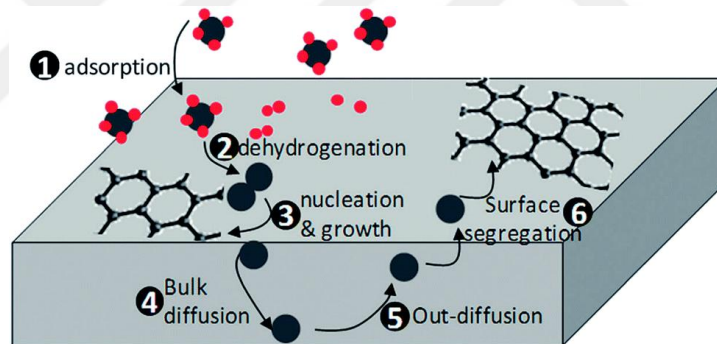
Figure 5: Schematic diagram of the graphene formation on a metal catalyst. [86].

2.2. Experimental processes for graphene growth

2.2.1. Monolayer graphene growth

We used a CVD furnace that has a quartz tube with a diameter of 11 cm (fig 6). The tube was baked at 1000 °C under a 500 sccm Ar flow for 2 hours before running the experiments. We placed a small piece of Cu foil inside the tube. The factors used to determine the purity of the gases during annealing were the purity levels of Ar and the H_2 sources. The procedure was then started by heating the CVD furnace to 1000 °C for 40 minutes, followed by an annealing phase at the same temperature, once the system has attained a pressure of 5×10^{-2} mbar. Only pure hydrogen and argon (99.999% each) were used to treat the Cu surface during the heating and annealing processes. After the annealing process was finished, we run methane (CH_4) gas. A needle valve between the pump and tube exhaust adjusted the pressure in the chamber. The gas flow rates were kept constant during the cooling of the CVD furnace.

2.2.2. Multilayer graphene growth

A larger CVD furnace and quartz tube was used for multilayer graphene growth. For every test, a 3×3 cm^2 Ni film, deposited on SiO_2/Si wafer was used. The ambient gases were removed by pumping the furnace for one hour. The system was flushed with Argon for 50 minutes while it reached 1000 °C. Subsequently, hydrogen and methane gases were added into the system. After this, the furnace was cooled down to room temperature for two hours. Number of graphene layers varies with the Ni film thickness, and the flow rate of H_2 and CH_4 gases.
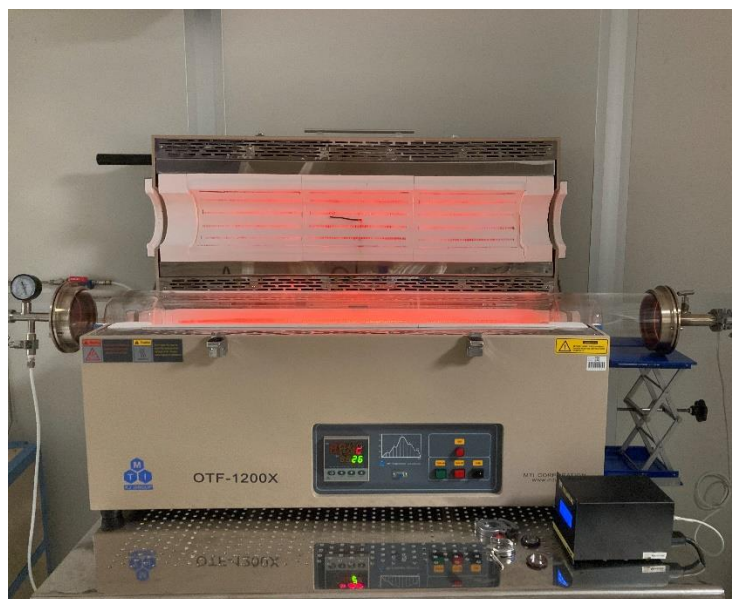
Figure 6: Experimental CVD setup for growing graphene on nickel film.

2.2.3. Transfer of monolayer graphene

In our experiments we chose the most widely used wet chemical etching and transfer process of CVD graphene. To prevent graphene from mechanical damage, wrinkles, and cracks, different support layers have been used. PMMA is one of the most common support layer for transferring graphene to the target substrate [87] because it has sufficient mechanical strength, is insoluble in water, has low viscosity, and is resistant to etching. [88] PMMA (MicroChem 950 PMMA 2% in chlorobenzene) was spin coated at a rotation speed of 4000 rpm for 45 seconds, forming a thickness of about 200 nm. The sample was baked at 180 °C for 5 minutes. Then the unintentionally grown graphene at the back side of the copper foil was etched by oxygen plasma. Next, the sample was immersed in a 0.1 M $((NH_4)_2S_2O_8)$ for one day to etch the Cu foil before being washed in (DI) water. The sample was rinsed four to five times with DI water. The graphene/PMMA layer was transferred to a SiO_2/Si substrate (300 nm thermal oxide). The sample is soaked into acetone for roughly a day to remove the PMMA coating, followed by rinsing with IPA and blowing with nitrogen.

2.3. Characterization of graphene

2.3.1. Optical Microscope

Optical Microscopy is the most common technique to inspect large area graphene samples before applying others such as Raman spectroscopy, AFM, or SEM. [64, 89] Graphene transferred on Si/SiO2 substrate is visible under optical microscope because graphene alters the interference color of reflected light relative to the empty substrate. The morphology of transferred graphene on SiO_2/Si resembles the morphology of graphene grown on nickel film. The contrast with graphene and substrate indicates a mixed structure of bilayer and multilayer graphene regions as shown in figure 8 below.
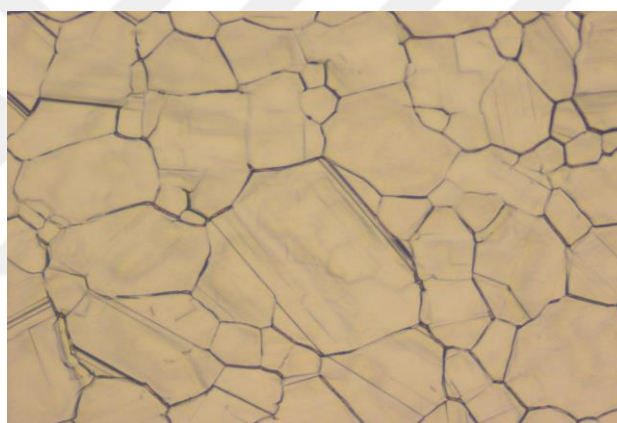
Figure 7: Optical microscope image of a monolayer graphene grown on Cu film by CVD. Sharp lines are copper crystal domains.
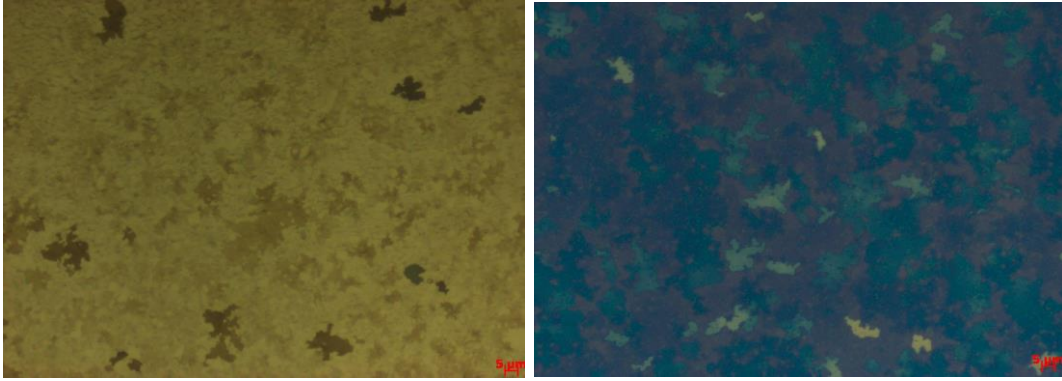
Figure 8: Optical microscope images of multilayer graphene grown on Ni film by the CVD technique and transferred on SiO2/Si substrate by the wet chemical process consisting of a mixed structure of bilayer and multilayer regions.

2.3.2. Raman spectroscopy

Raman spectroscopy is a nonlinear laser spectroscopy technique that provides information on the vibrational modes in a material by the inelastic scattering of a laser beam from a sample. Materails that contain carbons have modes in the range of 1000–2000 cm^{-1}. [90] Differences in Raman spectra versus changing the number of graphene layers suggests changes in the electron bands which help us to distinguish single and few layers of graphene. [91, 92] Raman spectrum is hard to distinguish from bulk graphite for more than 5 layers of graphene. G mode and 2D mode are the prominent features in the Raman spectra of graphene. The G peak is at 1580 cm^{-1} while the 2D peak is around 2680 cm^{-1}. Another peak called D peak which indicates defects can be found around 1350 cm^{-1}. The intensity, position and shape of the G and 2D bands varies with graphene layers which help us to determine the graphene film thickness.
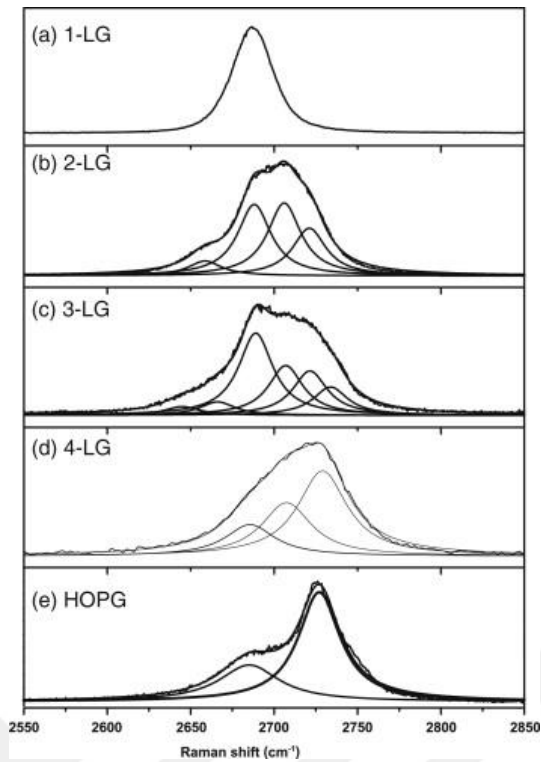
Figure 9: The measured 2D Raman band for different number of graphene layers with 2.41 eV laser energy. The Raman band splits as the number of graphene layers increases. The Lorentzian peaks used to fit the data are depicted by the lines beneath the peak. [92].

We utilized Raman (Renishaw inVia Reflex) in order to check the presence of graphene on metal (e.g. Cu, Ni) or after transfer. To avoid overheating the samples, we used a laser power at a low level of 5% of its maximum power.
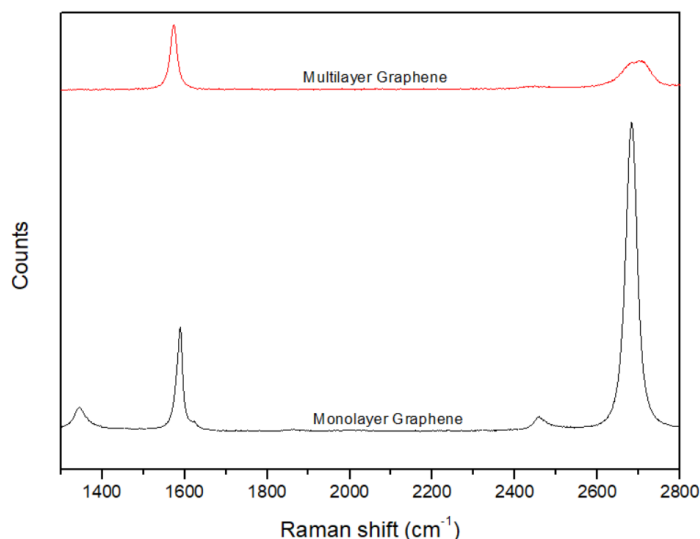
Figure 10: Raman spectrum of monolayer and multilayer graphene on Si substrate exhibiting distinct G (1588 cm-1) and 2D (2682 cm-1) peaks. The intensity of the 2D peak is larger than G by more than a factor of 2, which demonstrates high quality of the monolayer graphene and intensity ratio of less than 2 demonstrates multilayer graphene.

2.3.3. Determining number of graphene layers from UV-VIS spectroscopy

We also used UV-VIS transmittance of graphene transferred onto glass to determine the number of layers. The transmittance of graphene decreases as the number of layers increases. We measured the transmittance of a monolayer graphene film as 97.2%, which fits the optical absorption ~2.3% for monolayer graphene's theoretical value. [93] A nonlinear function $T = (1 + 1.13\pi\alpha N/2)^{-2}$ describes the transmittance of light through multilayer graphene in the visible range. [94] Here, N is the number of graphene layers and $\alpha = e^2/\hbar c \approx 1/137$ is fine structure constant. [66] The formula offers a straightforward method for counting the layers of graphene by measurement of light transmission.

Four different graphene films (growth time of 10, 20, 30, and 40 min) synthesized on 300 nm Ni film, were transferred to a glass and their transmittance was measured. The results show that the transmittance increases as growing time increase, indicating a reduction in the number of graphene layers. As 300nm Ni film is insufficient for more graphene layers because carbon accumulate more in the Ni film with longer growing times. Nickel is depleted during the growth time, resulting in fewer layers as the growth time increases.

14

Ni film thickness (nm)	Ar (sccm)	H$_2$ (sccm)	CH$_4$ (sccm)	Gr growth time (min)	% T in UV-VIS range	No. of layers
300	250	100	100	10	77	10.7
300	250	100	100	20	78	10.2
300	250	100	100	40	81	8.5

The multilayer graphene synthesized on 450 nm nickel film for 5 minutes growth time was transferred to a glass. A single transfer shows a transmittance of 75% indicating 12 number of graphene layers. In the figure 11 below, a 5 sets of these CVD grown graphene films stacked upon themselves yielded an average 40 layers of Gr. Gr grown on nickel gave irregular number of graphene layers which deos not increase linearly with the number of transfers. We explain this by non-uniformity of graphene film grown on nickel coated wafer. Graphene growth on corners of the wafer indicate few layers of graphene as compared to the center of the wafer as shown in the second transfer. 1, 3, 4 and 5 was transferred from the center of the wafer. We determined the number of these graphene layers from the transmission value observed at a wavelength of 550 nm. The discontinuity visible in the curves is due to switching of detectors.
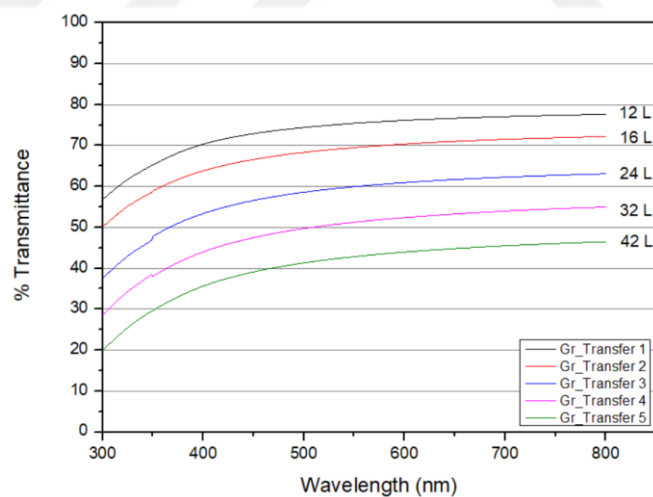
Figure 11: Transmittance of Gr films with up to 5 times transfer which yielded around 42 layers.

3. FABRICATION AND CHARACTERIZATION OF PDMS

3.1. Introduction

PDMS is a polymer that is suitable for numerous applications. The base polymer and the curing agent are the two components that make up the PDMS elastomer. They are combined in a specific volume ratio and begin to interact once they have been mixed together. Within 24 to 48 hours, the mixture can solidify at room temperature. Additionally, PDMS membranes with a thickness of around 250 µm can be cured in few minutes at elevated temperatures (RT < T < 200 °C). It has been reported that PDMS begins to decompose thermally at temperatures greater than 200 °C. [95] PDMS is elastic, transparent, biocompatible, gas-permeable, and makes conformal contact with surfaces. It is compatible with clean rooms. It also has high flexibility and a low curing temperature.

Table 2: Some relevant properties of PDMS (Sylgard 184, 10:1 base polymer to curing agent)

Characteristics	Value	References
Optical transparency	240-1100 nm	[96-98]
Surface tension	21-22mN/m	[99]
Glass transition temperature	-125°C	[99]
Elastic modulus	∼1–3 MPa	[100, 101]

PDMS can be micro-molded on silicon wafers using, for instance, spin-coating or spin-casting process, in which the PDMS film thickness depends on the rotational velocity. Additionally, vacuum or pumps can be used to direct the flow of PDMS over a master to create PDMS membranes. The cured PDMS membrane is carefully removed from the

silicon wafer and used as the stamp. The membrane would be unable to be removed from the substrate if the silicon wafer was not pre-treated, as the PDMS would form an irreversible seal with the silicon. Between the wafer and the membrane, there would be covalent bonds. One method for treating the surface of the silicon wafer is to put it through a fluorinated silanization process [102], where a molecular covering makes the substrate surface carry on like Teflon. As a result, the membrane and wafer do not form an irreversible seal. Adhesion forces and van der Waals forces now exert the greatest influence on the interaction between the silicon wafer and the PDMS membrane. The PDMS membrane may also be subject to electrostatic forces, or charge effects, that cause it to curl up, wrinkle, or stick to itself during peeling.

PDMS cross-link weight ratio, and curing time and temperature, can be controlled to produce PDMS materials with various mechanical properties. [101, 103-106] The mechanical effects of cross-link weight ratio have been documented. [107] The Young's modulus decreases with up to mixing ratio of 10:1 after which it is independent of the mixing ratio as shown in figure 13. This is because excessive cross-linker causes the PDMS to cure more slowly. As a result, the proportion of the base will be more in the PDMS, which means there will be more unreacted base polymer present in the PDMS, making the final product softer. The linear relationship between the resulting strain and stress in figure 12 below demonstrates the elastic nature of PDMS with 10:1 mixing ratio. Therefore, we used a 10:1 mixing ratio to get an elastic and softer PDMS films.
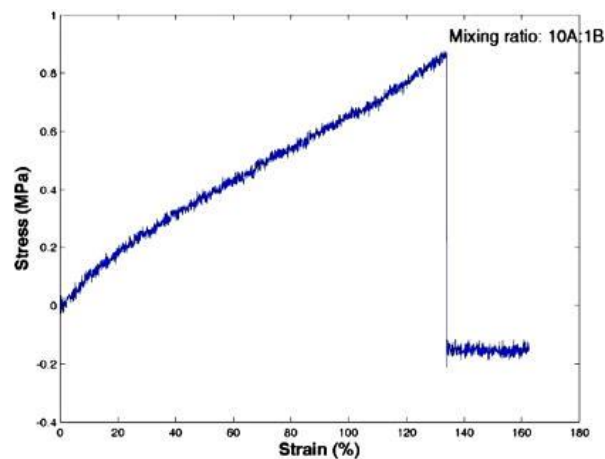
Figure 12: Stress strain relationship of PDMS with 10:1mixing ratio [108] The linear relation demonstrates the elasticity of PDMS.

17
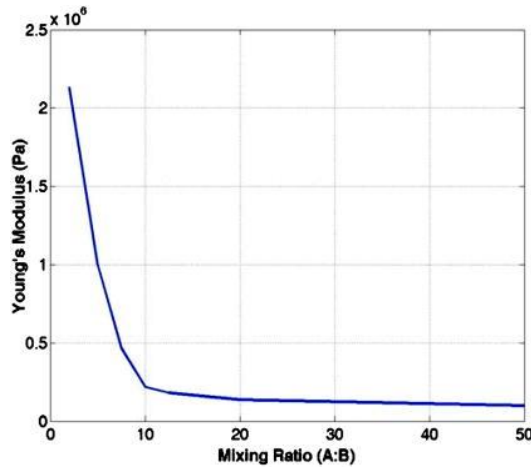
Figure 13: Relationship between Young's modulus and mixing ratio [108]

3.2.   Fabrication process

3.2.1. PDMS plain film casting

PDMS kit (Sylgard 184, Dow Corning) containing the base polymer and curing agent were used as received. PDMS was mixed for 10 minutes in a 10:1 mass ratio of the base polymer and a cross-linking agent in a mixing container. It was degassed under vacuum at 93 kPa for 40 min to remove entrapped air bubbles. Mixture was then spin-coated on a 4-inch silicon wafer at 100 rpm for 3 minutes to produce PDMS sheets with approximately 400 μm thickness. It was placed on a flat surface or a hot plate for 15 min at RTP before curing is started to reduce the edge bead. Curing is done at 70 °C for 3 hours. Then PDMS is gently peeled off from the wafer. The silicon wafer was initially coated with a fluorinated silane layer using RIE, C_4F_8 for 5 minutes with 70 sccm C_4F_8, 1 sccm SF_6, and 40 sccm Ar at 1W power beforehand to avoid adhesion of the PDMS films after curing.

18
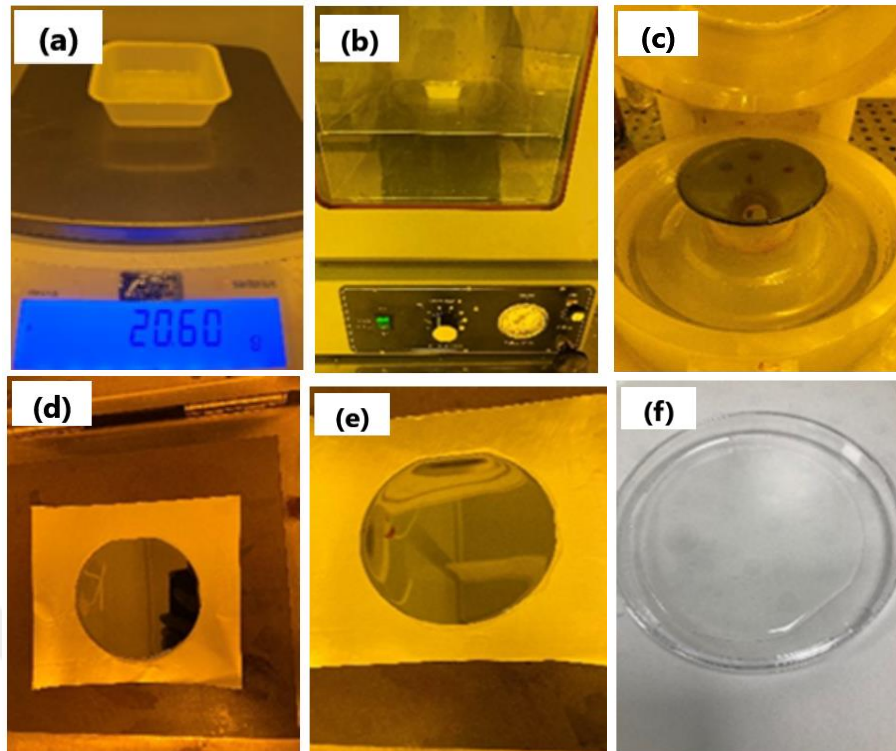
Figure 14: Work flow for PDMS synthesis, spinning, and annealing process. (a) mixed the elastomer and curing agent at 10:1 ratio (b) degassed under vacuum for 40 minutes (c) spin-coated liquid PDMS to the silicon wafer (d) put on a hotplate for 15 minutes (e) cured on a hotplate at 70 °C for 3 hours and (f) peeled off from the wafer

3.2.2. Optimization of plain PDMS film production recipe

To get desired results, it is important to produce uniform PDMS films with a certain thickness. While too thick film is hard to strain, too thin films tend to be non-uniform. Non-uniform thickness leads to non-uniform strain over the PDMS surface which would wash out the effect as periodicity would be uncontrolled.

After producing the PDMS films, their thickness was measured throughout the surface by cutting the film into 1 cm × 1 cm pieces using a blade along x and y radial direction as illustrated in Figure 15. Spin speed and time were controlled to achieve the desired thickness of the PDMS film. Figure 16 shows a relationship between the measured thickness of spin-coated PDMS at 100 rpm for two different spin time of 2 and 3 minutes with the radial distance. For the same spin speed of 100 rpm, 2 minutes of spin time shows a thickness of approximately 450 μm, whereas 3 minutes shows a thickness of around 350

μm. Hence, thickness and uniformity increase with increasing spin time. As a result, we chose a spin time of 3 minutes for our experiments. The thicknesses of different PDMS samples with the same parameters were measured to verify the consistency of a film thickness among the samples along a radial direction. The consistency of a 350 μm thick film spun at 100 rpm for 3 minutes is shown in Figure 17.
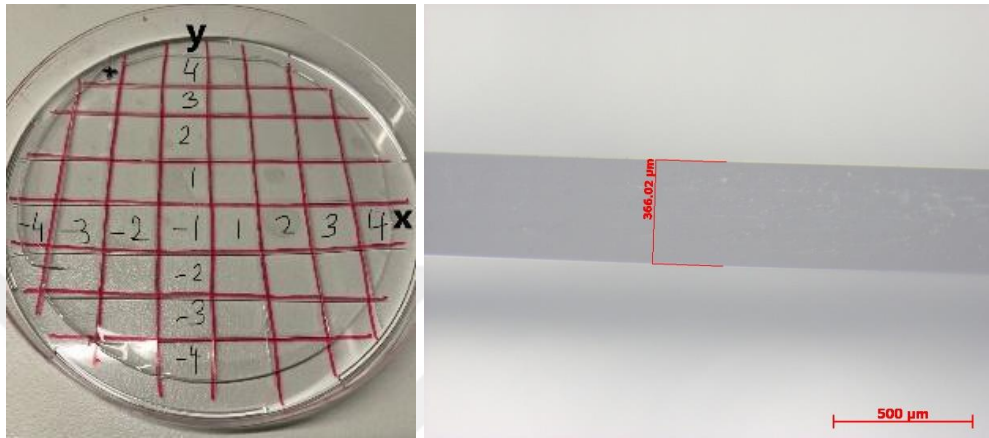
Figure 15: Peeled-off PDMS. Each marked number represents a 1 cm × 1 cm piece cut through a blade along x and y radial direction for measuring the thickness of the whole PDMS to ensure uniformity of the sample (left). OM image of cross-sectioned PDMS with thickness of 366 μm (right).
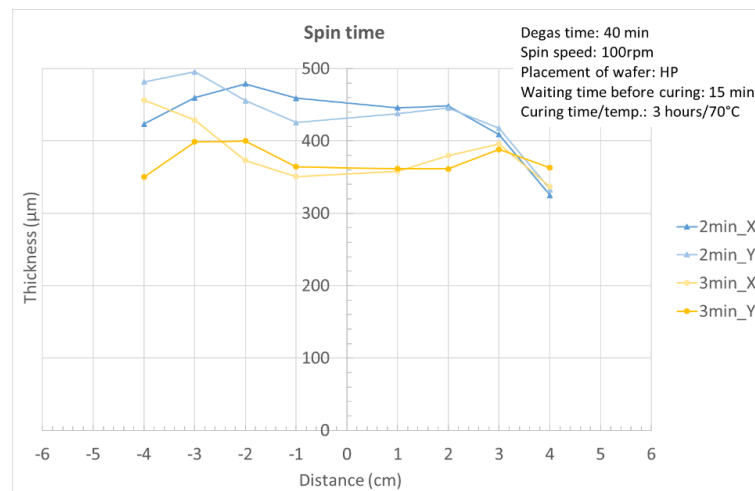
Figure 16: Thickness of PDMS versus distance from the center of the wafer for spin times of 2 and 3 minutes.
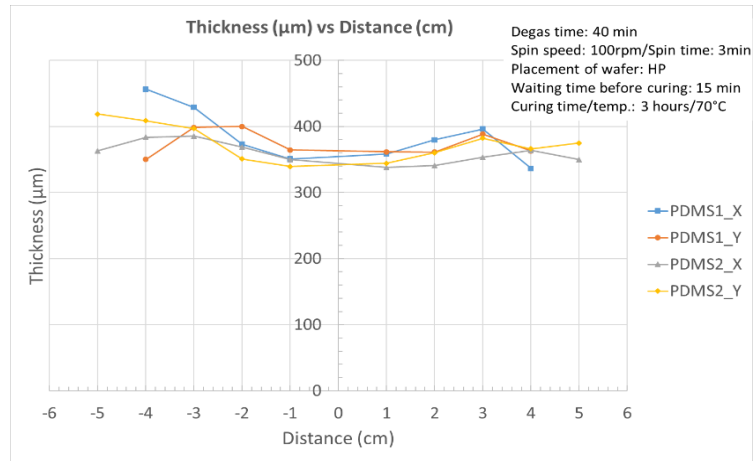
Figure 17: Consistency test for PDMS coating. Multiple samples were prepared with the same recipe and show very similar thickness distribution over the sample.

The loss of centrifugal force when spinning is stopped causes an abrupt change in the force balance. The Laplace pressure controls how the liquid moves and acts to diminish the curvature distribution and swiftly moves fluid from the side to the upper region because the substrate's curvature has a sharp gradient at the junction of its upper and side regions. This results in formation of a single edge bead shortly after spinning stops. As a result, the edge-bead affects the uniformity of the PDMS thickness distribution of the sample. We placed the spin-coated PDMS on a flat surface and rested for different durations before curing to analyze the edge-bead effect. Figure 18 shows the thickness of spin coated PDMS films prepared with resting times of 0, 7, and 15 minutes before curing. A smaller edge bead height was observed as the resting time was increased from 0 to 15 minutes. We observed that as the resting time is increased the edge bead advanced towards the center of the wafer due to the reflow of the PDMS before curing. Therefore, we chose to rest the PDMS films for 15 minutes before starting to cure them to avoid the edge bead effect.
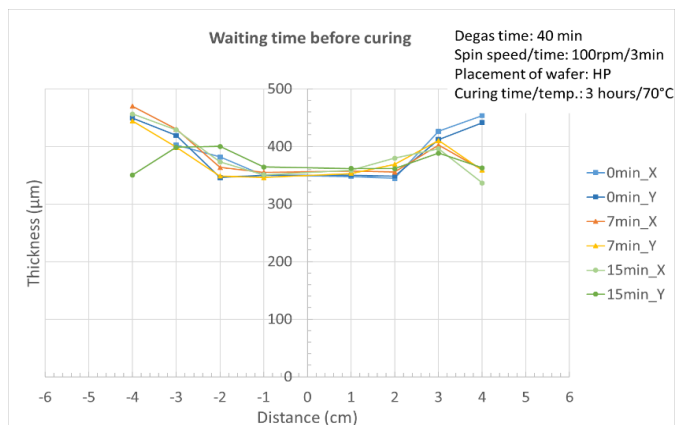
Figure 18: Edge bead reduction test. Samples were left still for settling before curing. Graph shows thickness versus radial distance of PDMS films with different resting times before curing. Longest resting time gave the least edge bead.

3.2.3. 3D patterned PDMS

Patterns formed on silicon wafers by electron beam lithography (see section 4.4.1) were used as molds to create a 3D patterned PDMS films. PDMS prepared with the process as described before (see section 3.2.1) was spin-coated on the silicon mold and was gently peeled off from the surface. Its pattern was the replica of the pattern on the Si mold. This approach of replica molding using PDMS provide us a platform to create patterned nano structures on flexible substrates using various designs.
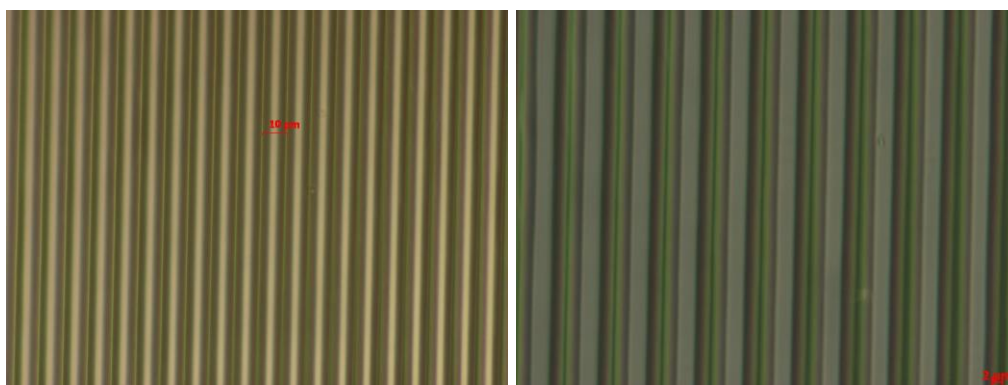
Figure 19: Optical microscope images of patterned PDMS with 10 μm pitch size fabricated using a silicon mold. Left image is the backside of the patterned PDMS and right image is the front side of the patterned PDMS.

3.3. Characterization of PDMS

3.3.1. Transmittance measurement

The optical properties of PDMS films depend on the surface structure and can also be tuned by applying tensile strain. We used a FTIR (Thermo Scientific Nicolet / iS10) to measure the transmission spectra of the films. Dry air was supplied into the instrument to purge the water vapor. The film was mounted on a sample holder with a hole through which an IR beam is passed and analyzed by an IR spectrometer. Transmission of the PDMS film at different strain levels measured by stretching the sample with the home-made stretching apparatus placed at the sample holder. Figure 20 and its inset below shows the measured transmittance of 350 µm thick unstretched and stretched PDMS film of sample size (3 cm × 3 cm). The unstretched spectrum of PDMS agree with the literature [109] and there is no data on the stretched PDMS film in the mid-IR range. The transmittance is tuned by the uniaxial stretching of the PDMS film. The transmittance increases with the increase in applied strain which means that the optical properties can be tuned by applied strain.
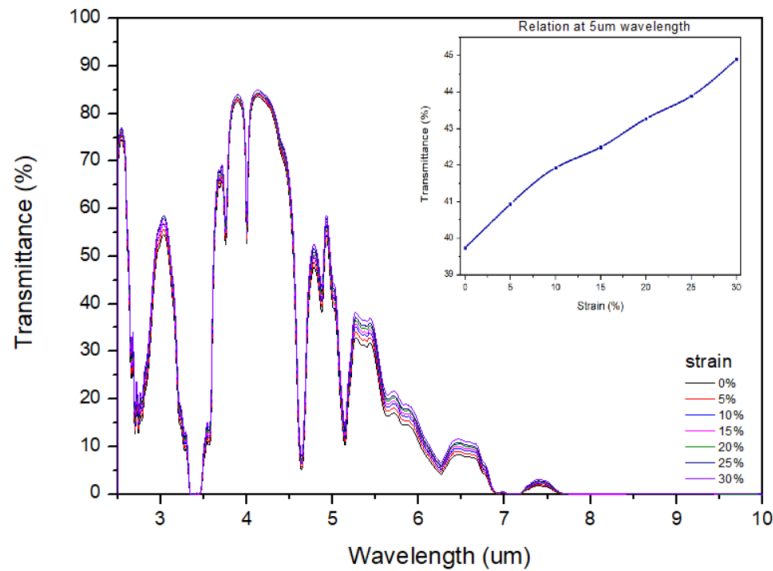
Figure 20: The transmission spectra of 350 µm thick PDMS film with different applied strains. It shows approximately a linear relation of transmittance with respect to strain, plotted for 5 µm wavelength above.
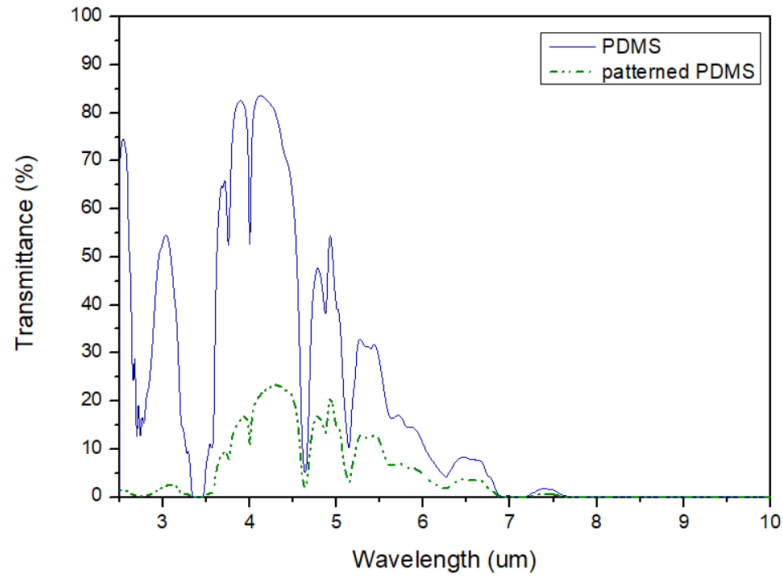
Figure 21: Transmittance spectra of 350 µm thick PDMS film and patterned PDMS film measured with FTIR.

Figure 21 compares the transmittance spectra of PDMS and 10 µm pitch size patterned PDMS of the same sample sizes (3 cm × 3 cm). In the case of patterned PDMS using transmission FTIR spectrum shows excessive drop in the transmission. The dramatic drop is caused by the reflection of light from the patterned surface. Therefore, portion of the light cannot reach the detector of spectrometer. Diffusive reflection of patterned PDMS films can be measured using an integrating sphere.

3.3.2. Emissivity measurements

Patterned PDMS films become diffusive in mid-IR range and most of the incident IR light ends up with diffusive reflection or scattering so that this portion of the light will not be counted in the transmission spectrum while it is not absorbed by PDMS either. Hence, it is impossible to estimate absorptivity directly from the transmitted IR light.

Therefore, we used an FTIR system equipped a dedicated emissivity option for measurements. The is located at Arçelik Research and Development Division in Çayırova, İstanbul. The operating principle of the system is based on extracting the emissivity of a given surface by comparing its radiation spectrum to the radiation

spectrum of a practical black body which has a temperature accurately matched to the temperature of the sample. The radiation spectra of the sample to black body are separately measured by the FTIR system. The ratio of the spectra after the background noise is subtracted gives the emissivity of the sample with respect to the wavelength.

Measurements were taken when the temperature was well stabilized for all of the samples. The emissivity was obtained by defining the ratio of the energy radiated from the sample's surface to that radiated by a blackbody furnace at the same temperature. The measured emissivities of flat PDMS and 10 µm pitch patterned PDMS of the same thickness ~350 µm at 150 °C is shown in Figure 22. Flat PDMS and patterned PDMS showed the emissivity values of 0.5 and 0.6 respectively. Although patterned PDMS with 10 µm pitch has slightly higher emissivity than flat PDMS, it showed no extra features around 10 µm wavelength.
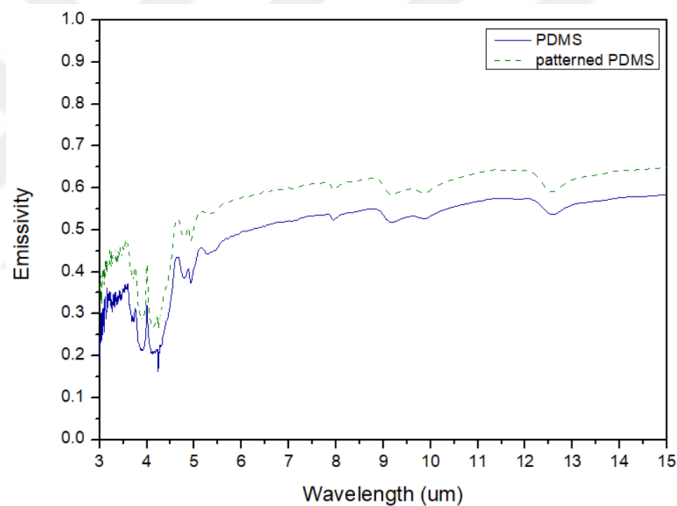
Figure 22: Emissivity measurement of the flat PDMS and 10 µm patterned PDMS measured at 150 °C. The patterned PDMS depicts the same emissivity profile as the flat PDMS.

The patterned PDMS was mounted on a sample holder and waited for three minutes before collecting the spectra for the uniform temperature of the sample. Emissivity of the 10 µm pitch patterned PDMS at 150°C with different percentage strain was measured by stretching the sample with the stretching apparatus attached on the sample holder.

Figure 23 and its inset below shows the calculated emissivity of 350 µm thick unstretched and stretched patterned PDMS of sample size (3 cm × 3 cm). So far there is no data on

25

the emissivity of the stretched patterned PDMS in the mid-IR range. The emissivity is tuned by the uniaxial stretching of the patterned PDMS. With the increase in strain, the amplitude of the pattern decreases. Stretched PDMS provides a better thermal contact to the adaptor as stretching PDMS is getting thinner and hence there was a less shield effect of PDMS against emission of thermal adapter. The intensity of the emissivity increases with the increase in applied strain which demonstrates that the optical properties of PDMS can be controlled by applying strain.
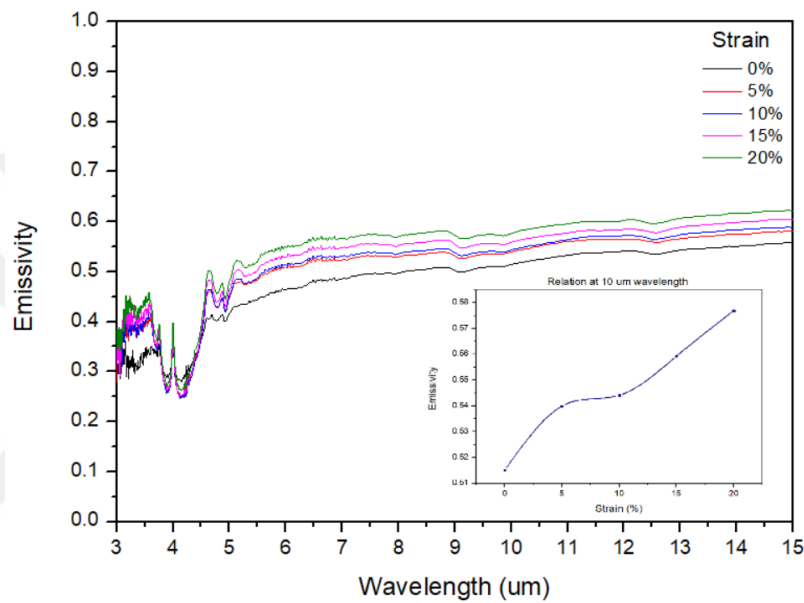
Figure 23: Emissivity of the 350 µm thick, 10µm pitch patterned PDMS with different applied strains. Emissivity increases with strain.

4.   3D PATTERNED GRAPHENE SURFACES

4.1.   Introduction

Flexible materials, such as PS and PDMS are utilized to provide morphology-controlled dynamic emissivity variations. Graphene was transferred on a PDMS substrate to attain longer pitch sizes [11]. Crumpled pitch can then be modulated by applying strain which is reversible during cyclical stretching and releasing [57]. Surface wrinkling has generated a lot of interest due to its ease of usage, applicability, and low cost. [110-113] However, the structures formed are random, resulting in the inhomogeneous strain distribution in each structure.

Micro and nanofabrication technologies have undeniably advanced over the last two decades from simple tools to lithography techniques to pattern materials for optics or electronics. Alternatively, these technologies are becoming more and more capable of creating and shaping micro or nanostructures from polymers or other molecular systems. Lithographic techniques like e-beam lithography [114-118] and nanoimprint lithography [119-123] enabled an extremely broad range of applications.

Two-dimensional honeycomb carbon lattice graphene can withstand up to 25% elastic deformation, as anticipated and later confirmed by measurement [124, 125], due to its mechanical properties of strong in-plane rigidity and huge elasticity. It is incredibly attractive to design patterns with graphene because of its special property as a highly anisotropic, atomically thin membrane with ultra-strength.

Graphene has been synthesized uniformly on a large scale using a CVD technique. [82, 126-129] As a result, a lot of experiments has been done on transferring graphene onto

planar substrates [82, 130-135] for the purpose of characterization of materials and device integration. 3D transfer onto micro-structured surfaces, on the other hand, has been difficult due to the possibility of graphene damage from high tensile stress during transferring.
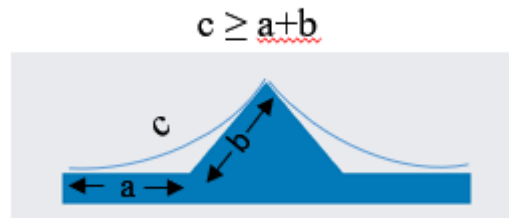
Figure 24: Gr doesn't follow the pattern of the pyramids. The length of suspended graphene is represented by c, and the lengths of the base and one side of the pyramid are represented by a and b.

The incorporation of graphene into three-dimensional structures like pillars and pyramids has been the subject of several previous studies. [136-139] Modified transfer methods, such as substrate-swelling and embedded polymer-assisted methods have also been investigated [140]. However, the graphene remains suspended as illustrated in figure 24 above. Pyramidal AFM tips with graphene coatings were made utilizing the PMMA wet transfer procedure, according to Lanza et al. [136] Winters et al. produced micron-sized trench-patterned graphene using a transfer printing technique. [138] The transfer of graphene onto 3D microstructures substrates has been shown in prior research, but only onto a small dimensions microstructure. [136] Using PMMA transfer and a solution of ethanol and water, Shim et al. showed how multilayer graphene could be transferred onto Si pyramids that were around 30 μm in height. [137] The uniformity and conformal contact of graphene onto 3D patterns, on the other hand, was not fully demonstrated.

The possibility of directly growing graphene films on pre-patterned substrates has been demonstrated in prior work using the CVD method to produce a few layers of graphene films on nickel-coated SiO_2/Si substrates. [141] Graphene films of various sizes and shapes can be synthesized onto the patterned nickel films. Patterned graphene films can be easily transferred to any substrate by etching nickel with $FeCl_3$ solution.

For graphene to successfully transfer to the chosen substrate, it is crucial to comprehend how graphene adheres to other materials. As is well known, the thickness and morphology of graphene are fundamental factors in its properties. Plasma [142-144] or ozone treatment [145-148] is the most common method for chemically altering the surface of graphene. The hydrophobicity of PDMS prevents graphene from adhering to the surface and causes folds. Therefore, surface modification of graphene is necessary for the uniform transfer of graphene on our patterned PDMS.

In an ultraviolet-ozone (UVO) environment, the degree to which the CVD growth graphene oxidizes is determined by the substrate that supports it. [149] Graphene was oxidized by ozone under UV exposure, converting C=C bonds into carbonyl C=O or hydroxyl-bonded sp^3 carbons (C–OH). [149, 150] The water contact angle tests further demonstrated that as UV irradiation time increased, the graphene became hydrophilic. [151] Oxygen adsorption and doping occur at shorter UVO exposures whereas longer exposures cause etching and the formation of significant defects. [147] The overall integrity and properties of multilayer graphene remains the same under UV exposure due to its lower inherent roughness [152] and effective screening of the substrate charge areas. [153] As a result, we can conclude that bilayer and few-layer graphene etching does not take place. [154] Therefore, when treating graphene with UV/ozone to make it hydrophilic. Hence, we exposed our patterned graphene for shorter period time of 30 minutes.

The option of growing graphene on nickel by CVD enabled the possibility of transferring graphene onto arbitrary shape surfaces. Here, flexible material, PDMS is utilized to provide morphology-controlled variations. Gr grown on a patterned Ni film was transferred on a PDMS substrate to attain longer pitch sizes. Our 10 µm continuous periodic patterned graphene on PDMS differs significantly from the previously reported studies that involved graphene transfer over small periodic pattern surfaces or large distance between patterns. Our fabrication methods focus on transferring direct graphene growth from a prefabricated mold of large pattern surfaces of 6 µm height with a pitch size of 10 µm onto a flexible substrate which can be periodically stretched and relaxed while preserving the integrity of graphene. By combining the advantages of both graphene and PDMS, we designed a large-scale flexible patterned material for the first time. These

3D graphene structures are continuous, crack free and large in dimensions than previously reported work. The spacing to height ratio of patterns is $0.08 < r > 0.33$ which usually results graphene either remains suspended or broken. We have demonstrated the capability to form different continuous 3D graphene structures of varying mold patterns by directly growing 3D graphene and spin-coating PDMS on it. The simplicity of UV ozone treatment allows the adhesion of graphene to PDMS via a simple and cost-effective process. Furthermore, we showed that the integrity of graphene remains crack-free up to 100% strain during stretching and releasing. Direct synthesis is not possible due to fragility of PDMS at temperature above 200 °C and wet transfer forms suspended graphene due to sharp and depth of the structure. The dimensions of our Gr films on PDMS are limited by the size of the stretching apparatus (SA) but scaling up can also be achieved. The graphene sheet fully covers the surface of the patterned PDMS which is analyzed using SEM and Raman spectroscopy.

4.2. Designing and manufacturing of the stretching apparatus (SA)

A home-made stretching apparatus (SA) was utilized to strain the PDMS samples. The SA for the project was designed by using Solid works and manufactured from aluminum and stainless steel. The dimensions of the stretching apparatus were chosen according to the limitations of the reactive ion etching (RIE) system. The SA can handle samples up to a maximum size of 3 cm x 3 cm and can be stretched by up to 100%. In order to test large sample sizes, a new SA with large dimensions can also be created. Figure 25 below shows the dimensions of our SA designed on Solid works. Figure 26 shows the mounted PDMS on the fabricated stretching apparatus.
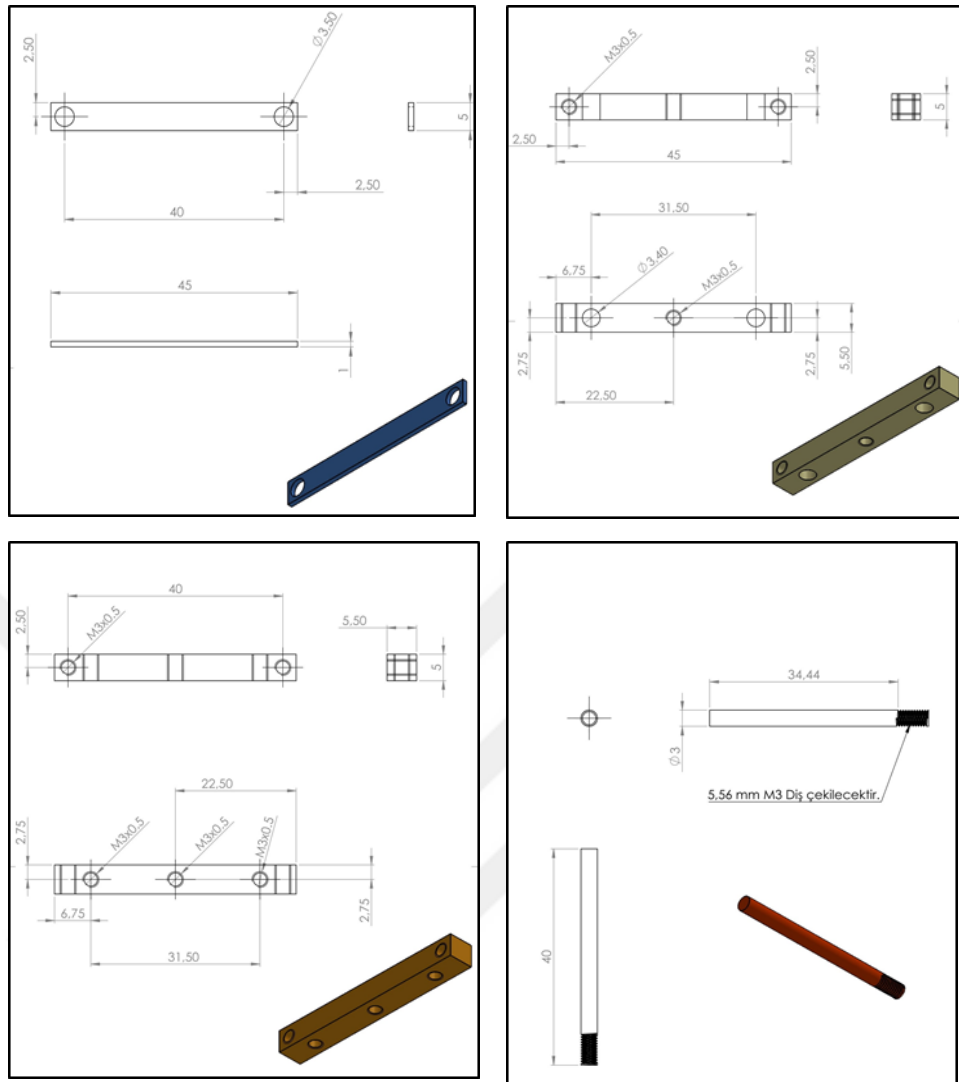
Figure 25: Design of the stretching apparatus (SA) with dimensions on Solid works

Figure 26: Mounted PDMS on a fabricated stretching apparatus. The sample's initial length before stretching is indicated by the letter L. Bar 1 is fixed and bar 2 moves as the M3 screw rod is turned to stretch the PDMS film.

4.3. Formation of 1D crumpled structure

4.3.1. Growth of CF_x on the pre-strained PDMS surface

PDMS film was cut into 3 cm $\times$ 3 cm size and clamped between two bars 1 and 2 of a stretching apparatus as indicated in figure 26 above. PDMS was uni-axially stretched by turning the center M3 screw to apply a pre-strain. Pre-strain was calculated by measuring the sample length (L) between bars 1 and 2 of the stretcher, before and after stretching, through the Vernier caliper. The tensile strain E = ΔL/L where ΔL is the change in length

of the sample before and after stretching. Pitch sizes were controlled by varying the tensile strain (E) at 5%, 10%, 15%, and 20%.

At high strain regimes, soft CF_x skin layers on stretched PDMS films prevented surface wrinkling from cracking. The soft skin doesn't form secondary structures up to the strain of 60%. Since the CFx skin layer has a 40-fold lower Young's modulus than comparable silica skin layers. it is considered a soft layer and thus resistant to crack formation. A soft CF_x layer with controllable thickness is deposited onto PDMS by the CHF_3 plasma gas. The skin layer over the substrate doesn't show any cracks up to 25% strain. [53]

Therefore, we treated the pre-strained PDMS, clamped on SA, with CHF_3 plasma gas for different deposition times at 50 sccm flow rate, 90 W of power and 50 mTorr pressure in a RIE system. Releasing the pre-strain formed the crumpled CF_x layer on PDMS. Figure 27 shows the as-fabricated and released PDMS which demonstrates the switching of orientation of the crumples. The CHF_3 RIE treatment time of 20 minutes, 30 minutes, and 40 minutes was used to obtain 3 μm, 4 μm, and 7 μm pitches respectively.
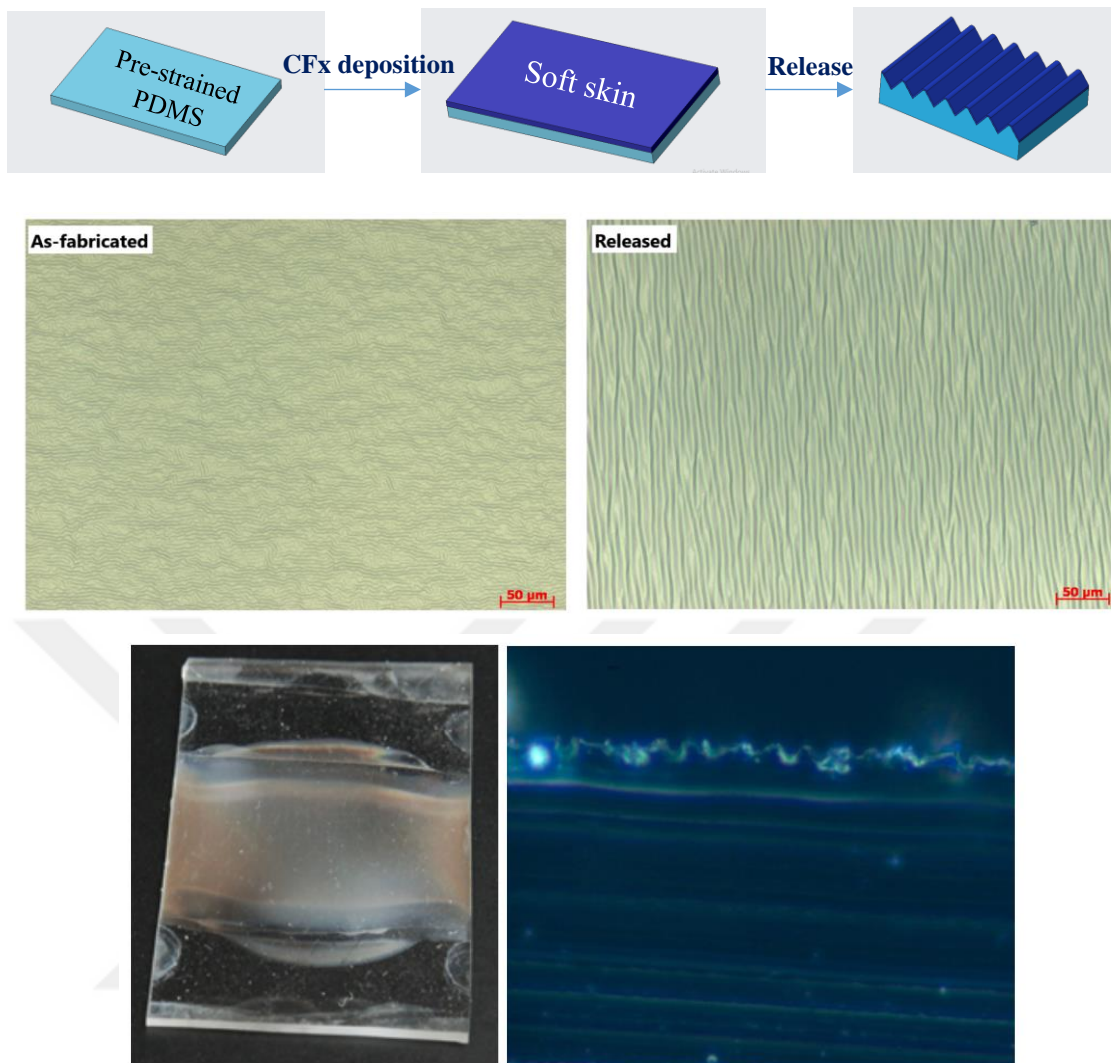
Figure 27: Schematic work flow of the CF_x growth on PDMS. Switching of CF_x crumples orientation after release of the PDMS film from the stretcher. Coated CF_x layer on the surface of the relaxed PDMS (left). Side view of the CF_x coated PDMS showing non-uniformity of the crumpled structures (right).

4.3.2. Optimization of pitch size by controlling the CF_x layer deposition parameters

CF_x layer was deposited on 3 cm × 3 cm pre-strained PDMS of 350 µm thick to prevent the surface from cracking during stretching and relaxing. The deposition time of the CHF_3 plasma treatment of the sample was varied to get the desired pitch size of around 10 µm. There was a uniform deposition of CF_x for 10, 20, 30 and 40 minutes after the release of the pre-strain. According to the experiments, pitch size increases with an increase in CF_x

34

deposition time, as shown in figure 28 below. Pitch size was measured at different points to ensure the uniformity of the pitch sized over the sample. The measured pitch size at these points is listed in Table 1 below.
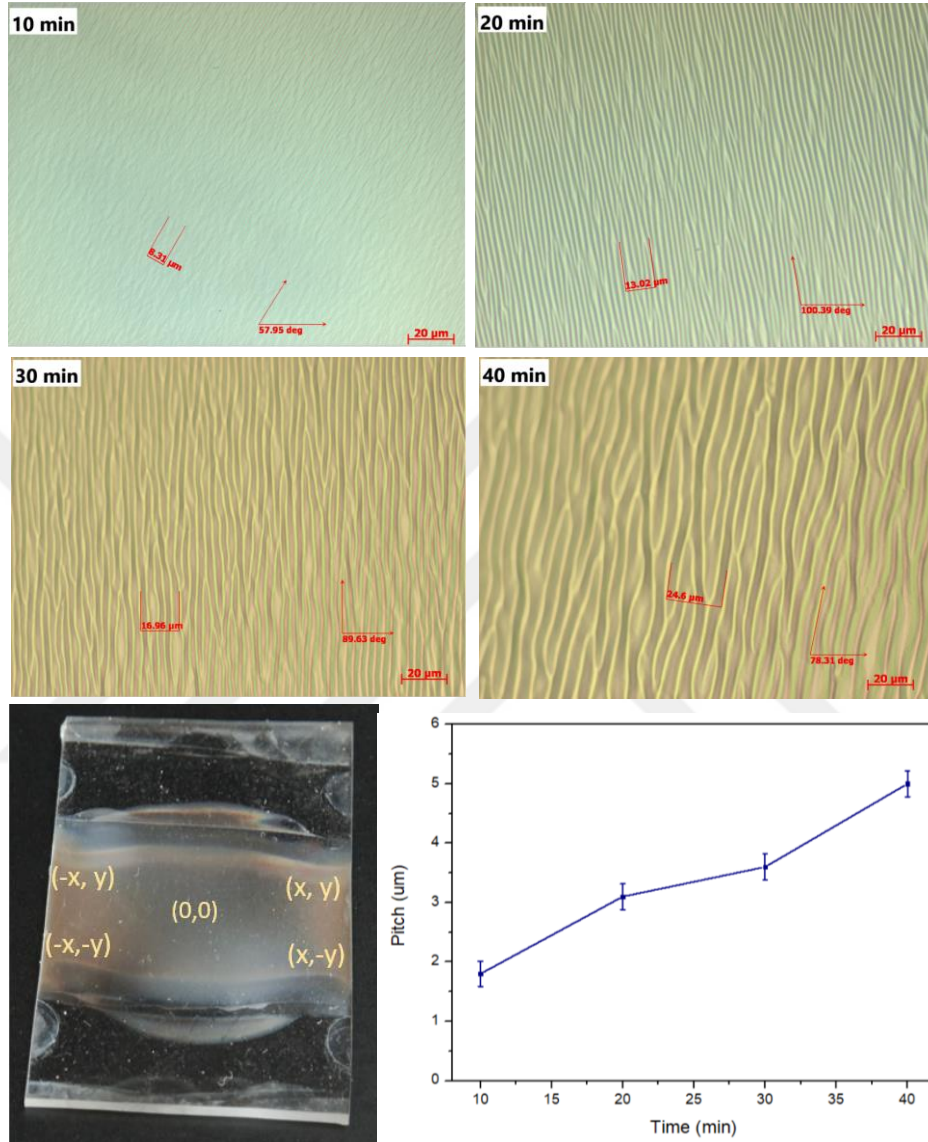
Figure 28: Optical microscope images of CF_x deposition under different growth time. Graph (right) shows the measured pitch sizes at different marked points on the sample as depicted in Figure (left). The standard deviation for more than 20 measurements is shown by error bars.

Table 3: Pitch size variation with the deposition time of CF_x. All other deposition parameters, amount of CHF_3 gas, power, pressure and sample strain were kept the same.

Pitch size (μm)	CFx deposition Time (min)	Strain of the sample (%)	CHF₃ (SCCM)	Power (W)	Pressure (mTorr)
1.8	10	20	50	90	50
3.1	20	20	50	90	50
3.6	30	20	50	90	50
5.0	40	20	50	90	50

Different percentage strains were also tested to achieve the uniform crumple orientation. The uniformity of pitch size at different pre-strain is shown in figure 29. To avoid contamination, cracks, folds and scratches over the sample during CF_x deposition, the RIE chamber was cleaned for 6 hours before the deposition of CF_x on pre-strained PDMS. There was a uniform deposition and orientation of crumples with 20% strain. However, the crumples were less ordered for low pre-strain values.
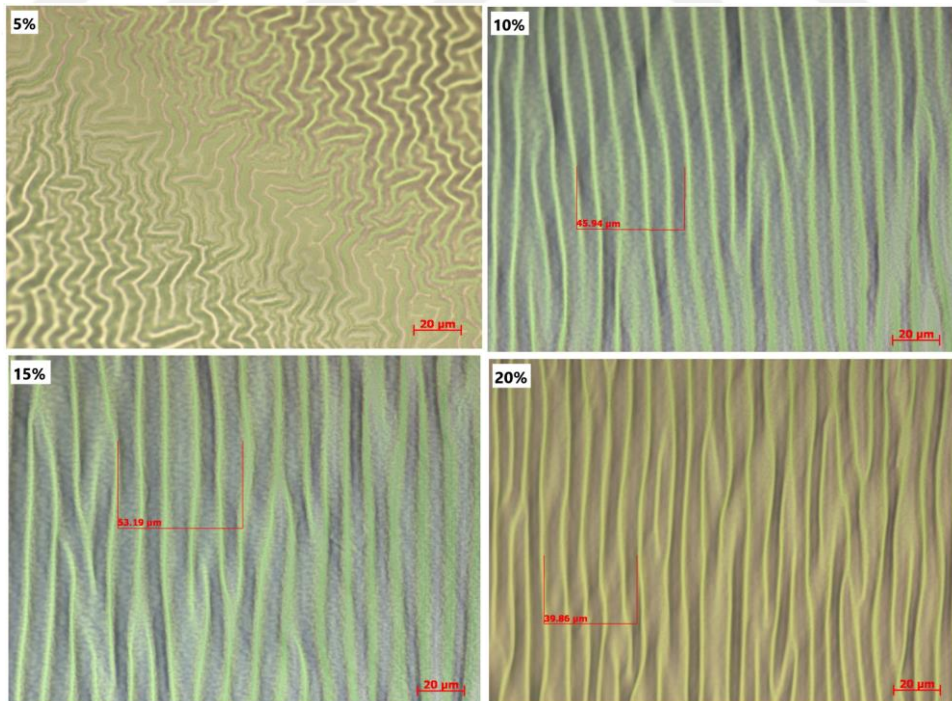
Figure 29: Optical microscope images of crumpled CF_x on PDMS under different pre-strain. Crumples aligned with the increase in pre-strain of PDMS

4.3.3. Transfer of graphene onto PDMS to form crumpled graphene surface

PMMA (950) film was spin-coated on Gr grown on Cu foil at 4000 rpm for 45 sec. The sample was heated on a hot plate at 170 °C for 10 minutes. Gr on the back side was etched by oxygen plasma in DRIE for a minute. The sample was immersed for one day in a 0.5 M $(NH_4)_2S_2O_8$ solution to etch the Cu foil before being washed in DI water. The Gr/PMMA layer was transferred to a pre-stretched CF_x coated PDMS sample and blow-dried with nitrogen. The stretcher loaded with the sample was left in an open air for around 12 hours. It was soaked in acetone to remove PMMA and rinsed with isopropyl alcohol (IPA). The strain on the sample was released to form crumpled graphene surface. However, graphene couldn't stick to the CF_x coated PDMS surface as it was removed during the blow-drying process. This method of creating crumpled graphene was unsuccessful.

4.4.   Formation of a 3D patterned graphene

4.4.1.   Preparation of a slilcon mold by electron beam lithography

The previous method of crumpling graphene by depositing the CF_x layer on PDMS gave inconsistent pitch sizes of the same parameters. Therefore, a silicon mold with uniform triangular ridges were first defined by an electron beam lithography (EBL) to get a predetermined graphene corrugation on PDMS. 300 nm thick layer of SiO_2 was deposited on (100) Si wafer by PECVD. It was heated at 150 °C for 2 min to dehydrate the surface. We coated a 300 nm thick CSAR 6200:13 EBL resist at 8000 rpm and baked the substrate at 150 °C for 2 min. We directly patterned the substrate by EBL with a dose of 275 uC/cm^2 considering the proximity effect correction. Patterns covering an area of 9 cm^2 typically took 3 hours of actual write time. The substrate was put in a developer 600:546 for 80 seconds, MIBK: IPA (1:1) (volume/volume) for 15 sec and IPA for 2 sec and then dried with compressed N_2. A 50 W oxygen plasma treatment was applied to the substrate for 8 seconds in DRIE to clean the residues of resist. The substrate was dipped in (BOE) solution for 5 minutes to etch SiO_2 and then into CSAR remover for 1 minute. 30%

TMAH was prepared by adding 18 g KOH in 42 ml H_2O and placed at 80 °C for 8 to 15 minutes to wet etch Si. The remaining SiO_2 layer was removed by BOE and then rinsed with DI and IPA.
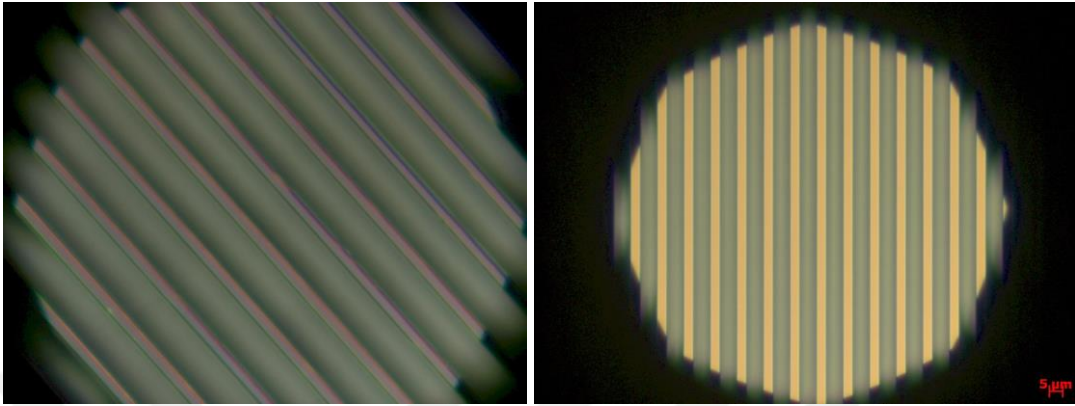
Figure 30: Optical microscope images of the mold with 10 µm period patterned by electron beam lithography.

4.4.2. Preapartion of the silicon mold by photolithography

EBL is expensive and slow, hence, a low-cost lithographic process that can generate nanostructures at a reasonable cost is needed. UV lithography is such a process. We prepared a one-time mask by EBL to be used multiple times for UV lithography. To create a mask, a Quartz substrate was spin-coated with ZEP 7000 resist and patterned with EBL. The substrate was dipped in (Ethyl methyl ketone: Anisole = 135:15) (V%: V%) solution for 1 minute. It was then dipped in (MIBK: IPA = 1:1) (V%: V%) solution for 10 seconds. It was sonicated in IPA for 30 seconds and dipped in chrome etchant until visible. Later washed with DI water and IPA. The substrate was put in (sulfuric acid: hydrogen peroxide = 90:30) (V%: V%) solution and then dipped in water, and rinsed with IPA again.

(100) Si wafer with 300 nm SiO_2 oxide layer was spin-coated with AZ 5214E photoresist at 4000 rpm for a minute and baked at 110 °C for one minute. It was exposed with patterns by photolithography using the Quartz mask. The patterns had various periodicity of 8 µm, 10 µm, and 12 µm. The wafer was put in AZ 726 MIF developer for 45 seconds and rinsed with DI water. The exposed SiO_2 patterns were etched by buffered oxide etch (BOE) for

5 minutes, acetone for 3 minutes and rinsed with IPA. The substrate was then etched by a wet etching solution, KOH at 80 °C for 6 minutes to form patterns.
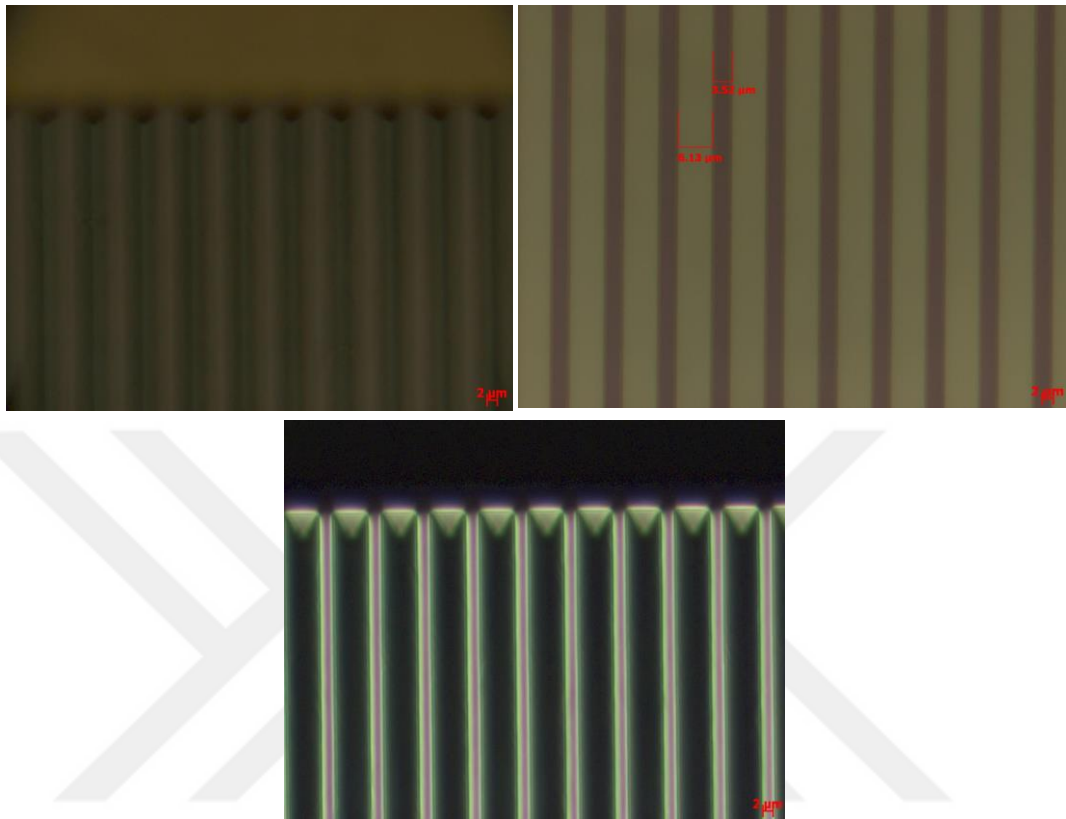
Figure 31: Optical microscope images of the mold with 10 μm pitch size designed by photolithography

4.4.3. Different surface modifications of patterned PDMS for adhesion of graphene

SEM images below show that graphene either remains bonded to the substrate or de-bonds from the substrate and is suspended on the target patterned substrate. The transferred graphene (see section 2.2.3) on a pre-strained patterned PDMS was often broken around the patterned structures after release of PDMS from the stretching apparatus (SA). Due to the elasticity limit of PDMS, when graphene was transferred on the patterned PDMS, its area was less than that of the stretched patterned PDMS. Due to the fact that unstrained graphene can't fully follow the maximum stretched patterned PDMS, there was a topological mismatch between the two surfaces. As a result, graphene breaks during the drying process. Moreover, the hydrophobicity of PDMS prevents graphene from adhering to the surface and causes folds. Therefore, surface modification of PDMS was necessary to improve wettability and stability for the uniform transfer of graphene. Various surface treatments including O_2 plasma, UV ozone treatment, and APTES solution were experimented on the surface of patterned PDMS before transferring graphene.
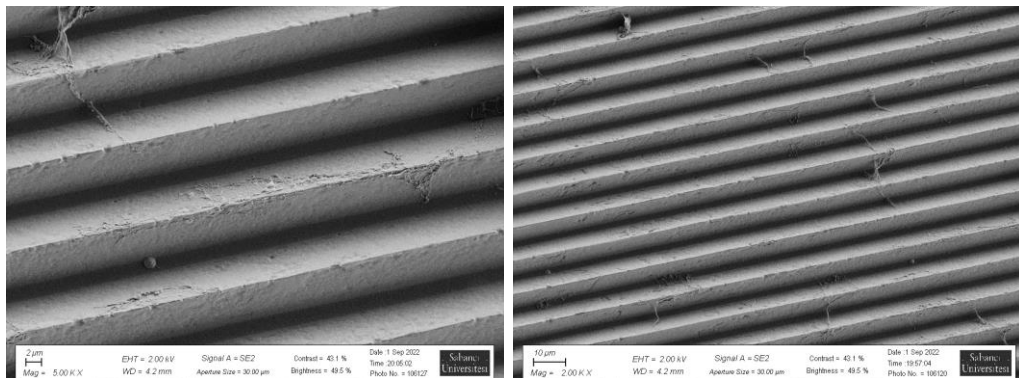
Figure 32: SEM Images of graphene on patterned PDMS surface indicating folds and suspended graphene. The transferred graphene is broken around the pre-patterned structures.
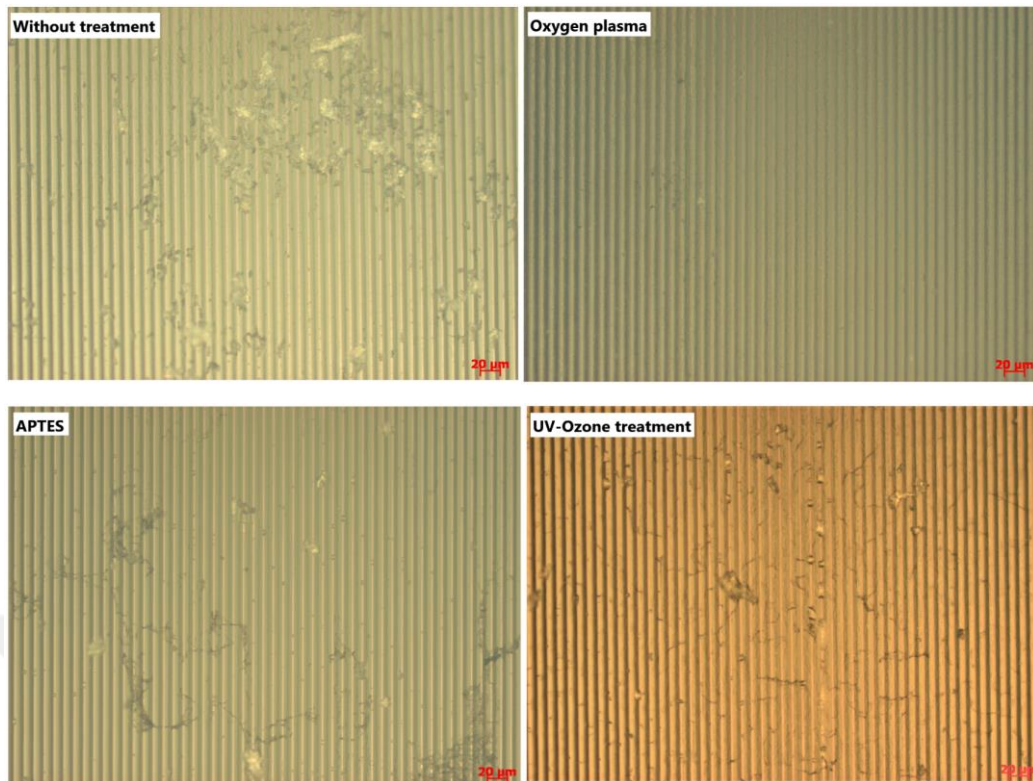
Figure 33: OM images of transferred graphene on patterned PDMS modified with different surface treatments. UVO provides better adhesion of graphene.

Raman spectrum of graphene on patterned PDMS, treated with O_2 plasma, UV ozone treatment, and APTES solution, was measured as illustrated in figure 34 below. The APTES solution and the oxygen plasma treated sample show no graphene peaks. Raman spectra of UV Ozone treated patterned PDMS surface indicate the presence of graphene (G peak 1600 cm^{-1}, and 2D peak 2700 cm^{-1}). Thus, UV ozone provides better adhesion of graphene than other surface treatments.
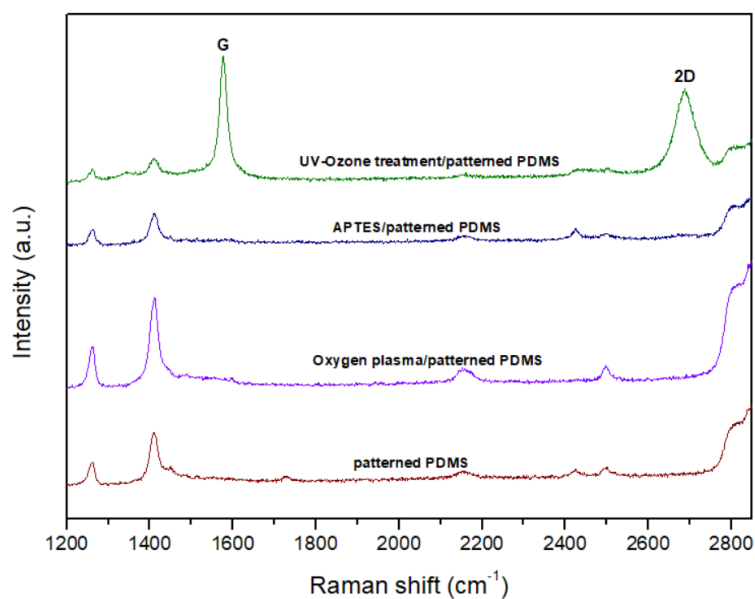
Figure 34: Raman spectra of Gr/patterned PDMS that is modified with different surface treatments before transferring graphene. PDMS exposed under UV-Ozone provides better adhesion of graphene on the surface.

4.4.4. Growth of 3D graphene on pre-determined mold

Another experimental approach was utilized to adhere graphene uniformly on the surface of patterned PDMS. We used the patterned mold fabricated by electron beam lithography (see section 4.4.1). The 850 nm Ni film as deposited by e-beam evaporator on a 1µm SiO_2 layer deposited by PECVD on the mold. Multilayer graphene film with 10 minutes growth duration was synthesized on $Ni/SiO_2/Si$ mold through CVD and then the substrate was exposed with UV ozone for 30 min. The PDMS that we prepared (see section 3.2.1) was then spin-coated on the substrate at 100 rpm for 3 minutes and cured at 70 °C for 2 hours on a hot plate. The edges (1mm) of the substrate was cut with a blade and dipped in BOE solution to etch SiO_2. Within few hours, the PDMS/Gr/Ni stack separated from the Si mold. PDMS/Gr/Ni stack dipped in 1M HNO_3 to remove the Ni. The remaining patterned PDMS/Gr was rinsed three times with DI water.
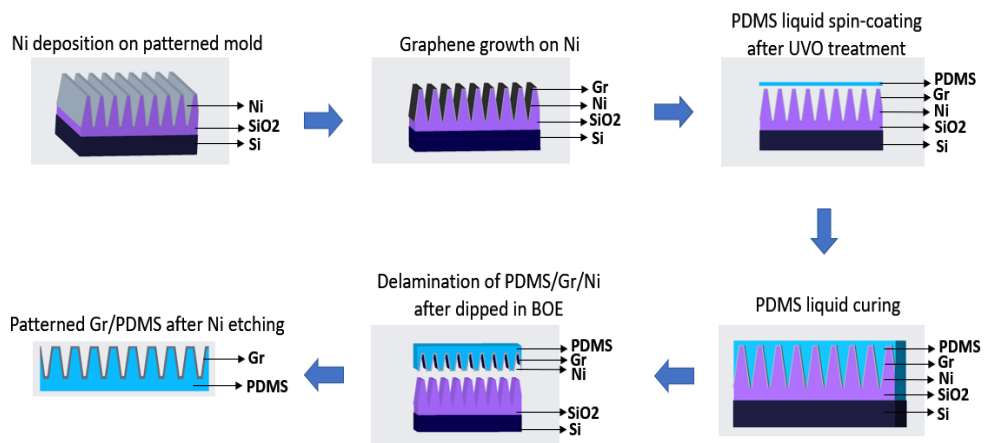
Figure 35: Schematic diagram on the formation of 3D Gr on PDMS.
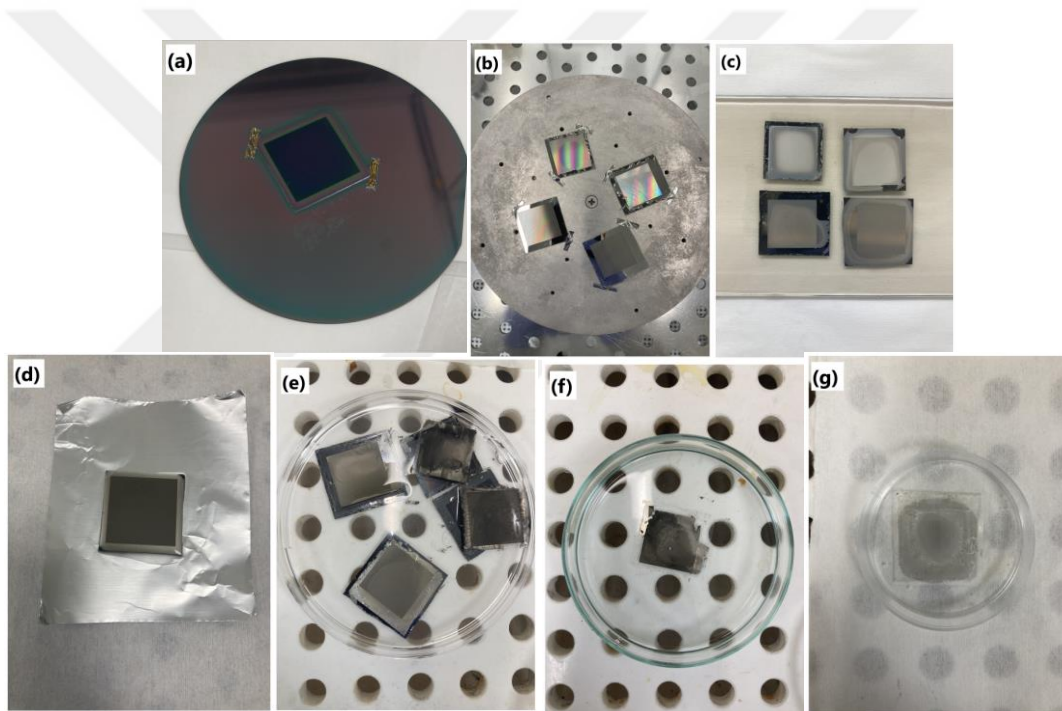
Figure 36: Experimental workflow of the deposition, growth, etching and transferring process of graphene on patterned PDMS. A patterned graphene film was synthesized on Ni/SiO2/Si mold via CVD. PDMS was spin-coated on Gr treated with UV ozone followed by etching of SiO_2 and Ni with BOE and HNO_3 respectively, leaving floating patterned graphene film on PDMS.
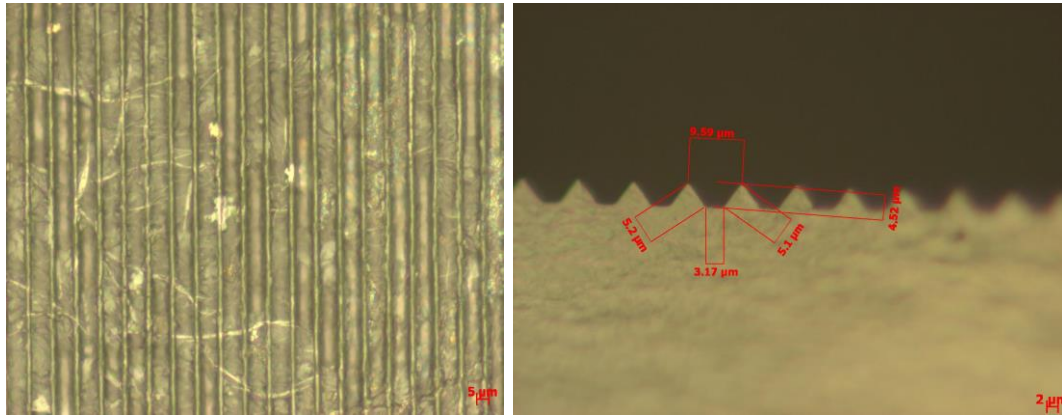
Figure 37: Optical microscope images of the front and side view of 10µm pitch size graphene on patterned PDMS

4.4.5. Patterning graphene with electron beam lithography (EBL)

In this experiment, we utilized EBL technology to fabricate graphene patterns. Large area multilayer graphene grown by CVD was transferred on a 400 nm Ni film substrate with a 300 nm SiO_2 layer on Si using PMMA assisted wet transfer process. After four times transfer of graphene film on to Ni substrate to form around 45 layers of graphene. After the removal of PMMA, the e-beam resist, CSAR 6200: 13, was spun at 4000 rpm for 45 sec onto the graphene substrate and soft bake at 150 °C for 2 minutes on a hot plate. The substrate was patterned with EBL and the desired pitch size can be determined by the mask. After patterning, the substrate was dipped in a developer 600:546 for 40 seconds and (MIBK: IPA = 1:1) (V%: V%) solution for 20 seconds and IPA for 10 seconds. After that, the graphene exposed to air was etched away using O_2 plasma at 100 W for 2 minutes. Then, CSAR remover was utilized to etch the resist away.
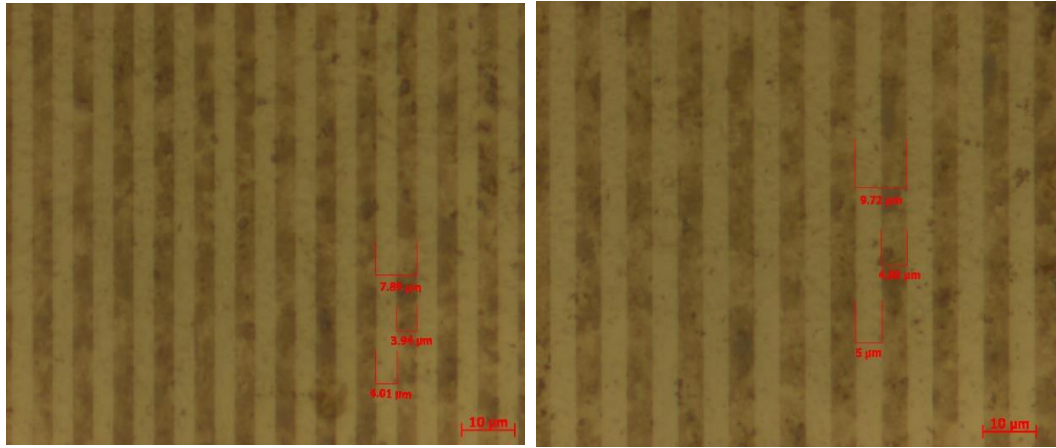
Figure 38: Optical microscope images of 8 µm and 10 µm pitch size patterned multilayer graphene on Nickel substrate with EBL.

4.4.6. Spontaneously corrugated Ni/PDMS film

We designed a structure comprised of a deposition of Nickel film of low emissivity on atop of PDMS of high emissivity. The Ni films on PDMS were prepared by electron beam evaporation. The coexisting of periodic surface patterns and cracks are formed on the sample. The deposition time determines the pitch size of the patterns. Different Ni thickness yield different pitch size. In general, small Ni thickness, 30nm, gives irregular patterns over the entire film. When the Ni thickness increases, the periodic surface patterns are induced. It is observed that the pitch size of around 10µm and 20 µm are observed for 100nm and 200nm Ni thickness. The induced patterns depend on the Ni film thickness. If the Ni thickness is large, cracks formed on the surface of the film. The cracks are narrow at low Ni thickness. The width of the cracks increases with the Ni thickness. In the experiment, we also modify the pitch size of the patterns by applying strain, parallel and perpendicular to the induced patterns. We suggest that the occurance of induced surface patterns and cracks are formed due to the thermal stress of PDMS during the Ni deposition as the temperature of the PDMS increase during deposition. After deposition, the PDMS cools down and thermally contracts, forming the induced Ni patterns. The induced surface patterns are aligned perpendicular to the cracks. The topography is characterized by dispersed cracks that change in size with applied strain, allowing the exposure of the beneath PDMS.

45
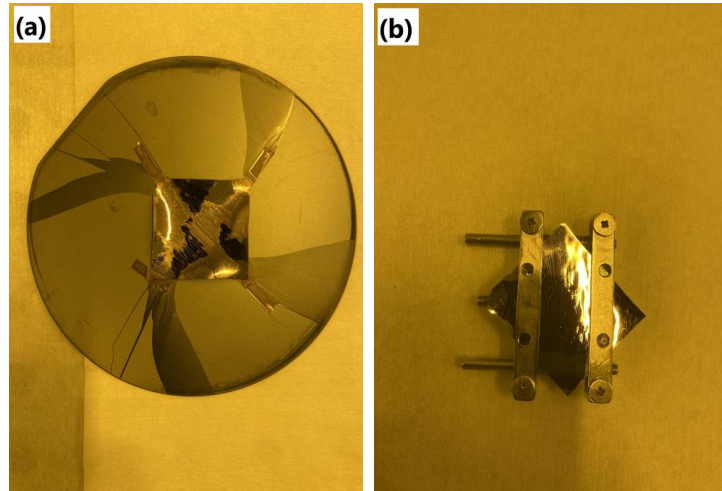
Figure 39: Ni film is deposited on PDMS with electron beam evaporation causing induced surface patterns and cracks. After deposition, strain is applied to change the pitch size and crack widths through the stretching apparatus (SA).
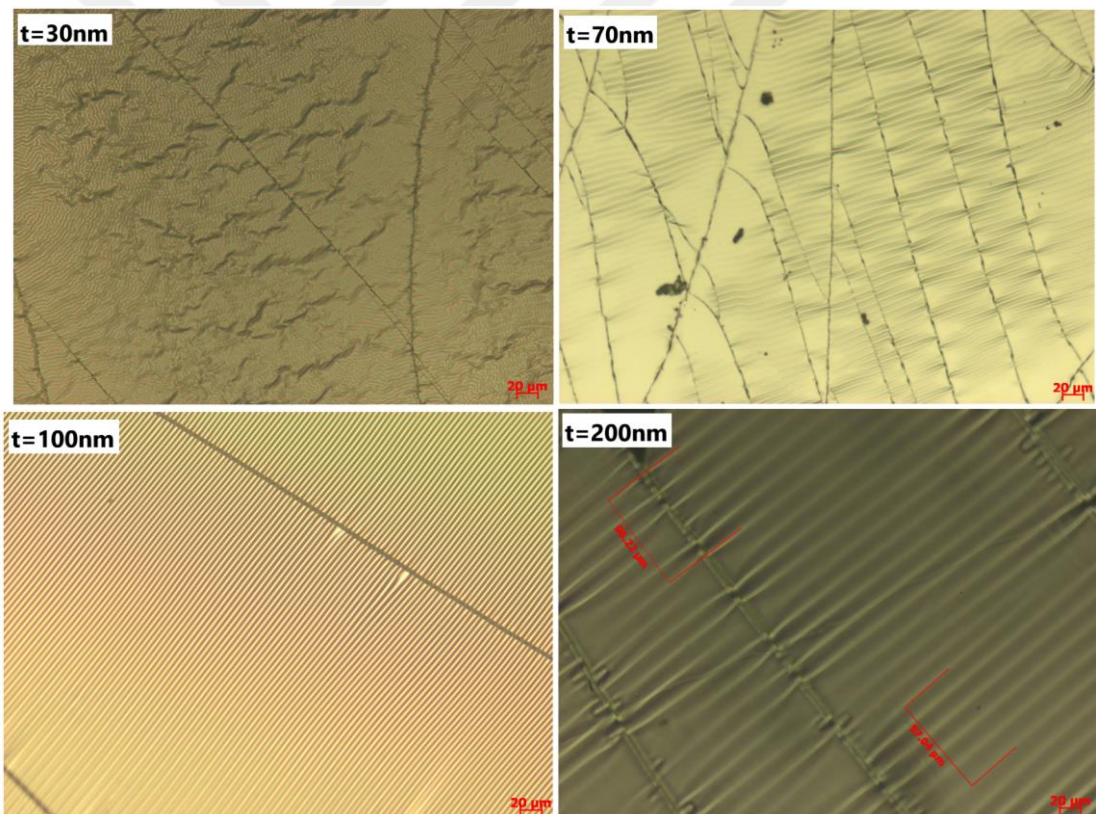
Figure 40: Optical microscope images of nickel films deposited on PDMS with thicknesses t = 30, 70, 100, and 200 nm forming spontaneously corrugated structures. Thinner nickel films show irregular structures and thicker films show periodic structures but more cracks at the same time.

4.4.7. Fabrication of patterned Ni-SiO₂

We designed a patterned Ni-SiO$_2$ of 8, 10, 12, 14 µm periodicity using EBL. First, 300nm SiO$_2$ layer was deposited on a Si wafer. The e-beam resist, CSAR 6200: 13, was spun at 4000rpm for 45 seconds on the substrate and bake at 150°C for 2 minutes. The substrate wasa patterned with EBL of various periodicity. After patterning, the substrate was dipped in a developer 600:546 for 40 seconds and (MIBK: IPA = 1:1) (V%: V%) solution for 20 seconds and IPA for 10 seconds. After that 300nm Ni was deposited.
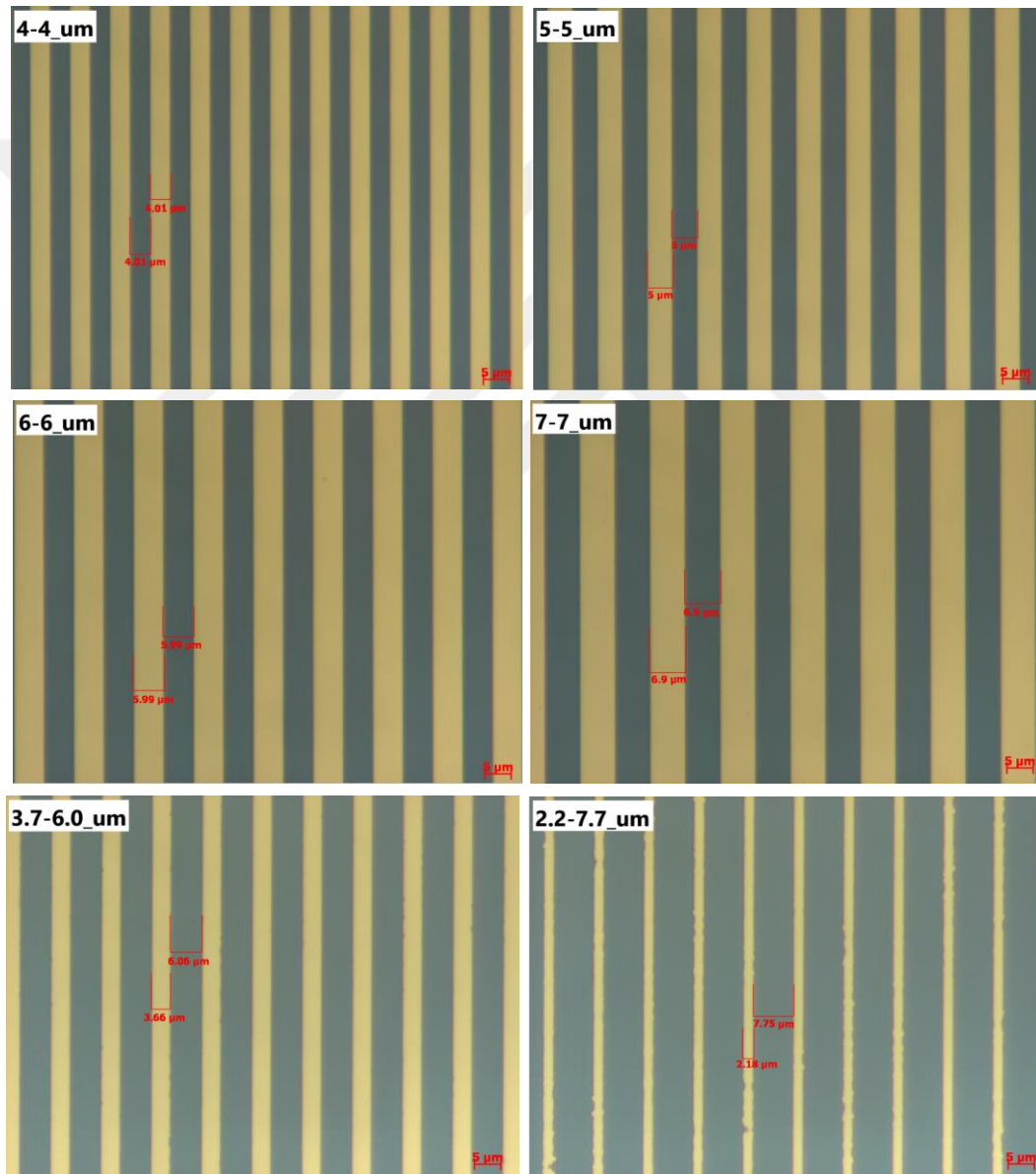
Figure 41: Patterned Ni-SiO$_2$ of various periodicity designed through electron beam lithography.

4.5. Characterization of a patterned graphene

4.5.1. Raman spectroscopy

The Raman spectra were taken to check the presence of graphene on PDMS. The PDMS peaks between 1250-1450 cm^{-1} and between 2800-3000 cm^{-1}. Peaks at 2D (2700 cm^{-1}) and G (1580 cm^{-1}) shows existence of graphene on patterned nickel film and PDMS. Different spots on the patterned graphene/Ni yield different ratios of 2D/G peak intensity. The ratio value above 2 indicates monolayer graphene and below 1 indicates at least two layers. Thus, our graphene consists of monolayer, bilayer and multilayer graphene areas. The lack of a D band (1350 cm^{-1}) confirms a high-quality defect-free graphene growth. Raman spectra on PDMS was also taken at different spots on the surface. Thus, Raman indicated the successful transfer of graphene from patterned Ni film to patterned PDMS, consisting of monolayer and multilayer graphene, over the whole sample as shown in figure 43.
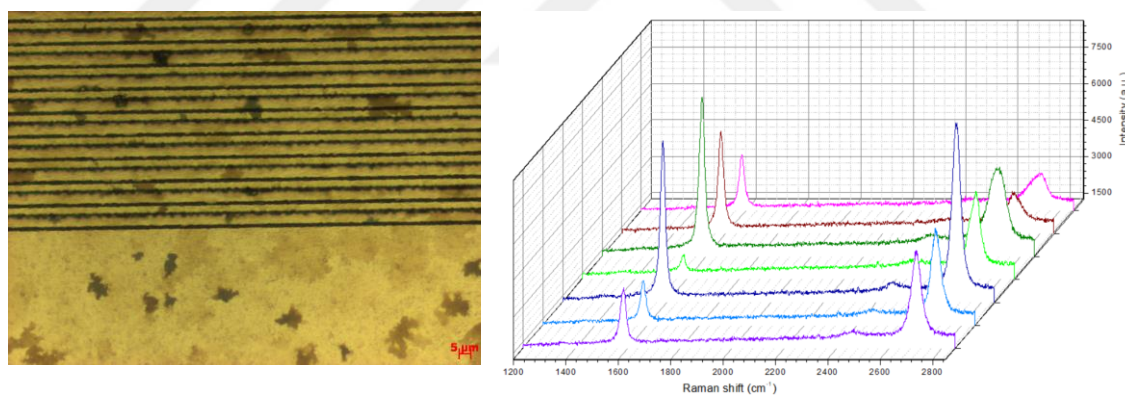
Figure 42: Optical Microscope Image of the graphene growth on patterned Ni film. The contrast with graphene and substrate indicates a mixed structure of bilayer and multilayer graphene regions. (left) Raman spectra of graphene on patterned nickel film, exhibiting distinct G and 2D peaks. The intensity ratio of 2D/G peak has different values, which indicates that our multilayer Gr has mixed structure. (right)
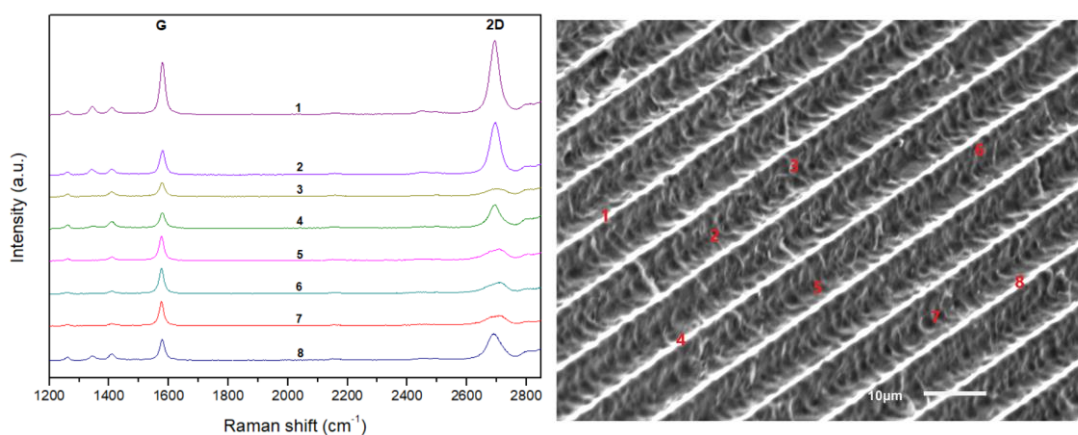
Figure 43: Raman spectra shows the successful transfer of graphene on patterned PDMS measured at different points marked on the sample.

4.5.2. Scanning electron microscopy

SEM measurements were conducted to characterize the morphology of the patterned graphene on PDMS. SEM images of patterned PDMS covering multilayer graphene are shown in figure 44. Each pattern is about 6 µm height with a pitch size of 10 µm. It can be seen that the multilayer graphene covering on PDMS retains good integrity. The surface morphology of PDMS is similar to that of patterned nickel. This indicates that the as-patterned graphene pattern on PDMS uniformly retains the structure of the patterned nickel film. The periodicity of graphene pattern is determined by pitch size of the patterned nickel, which is then determined by that of the photomask applied in the photolithography process. Large graphene area films can also be fabricated by preparing large size Si mold.
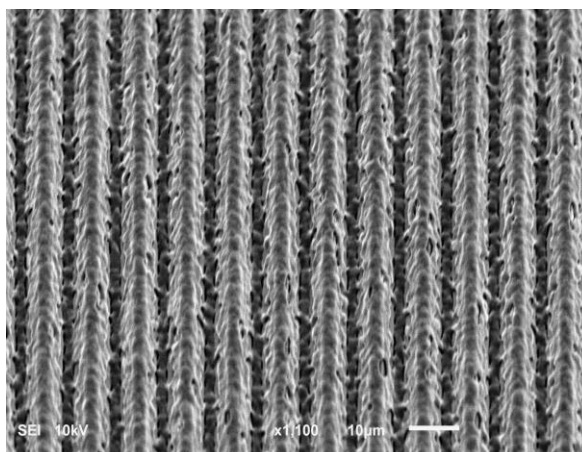
Figure 44: 30° tilted SEM image of multilayer graphene growth on patterned nickel film of 10 µm pitch size
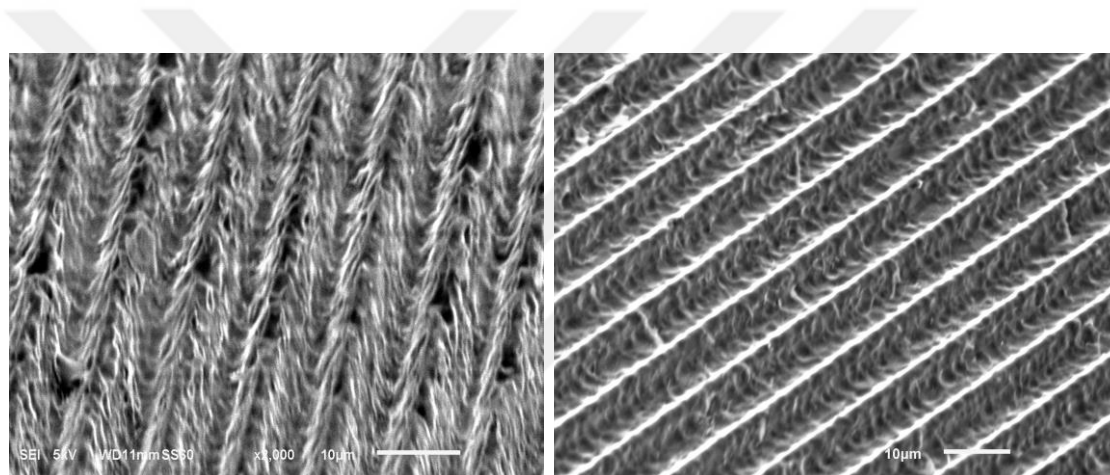
Figure 45: 45° tilted SEM images showing the central region of the patterned graphene of 10µm pitch size on the PDMS substrate

Figure 46 below shows SEM of unstretched graphene of a pitch size of 9.4 µm taken from the center of the sample. The original and stretched lengths of the sample in the stretcher are 11 mm and 16 mm, respectively. After 45% tensile strain (E) of the sample in the stretcher, the pitch size of the graphene at the center increased from 9.4 µm to 13.35 µm, which indicates a 42% strain.
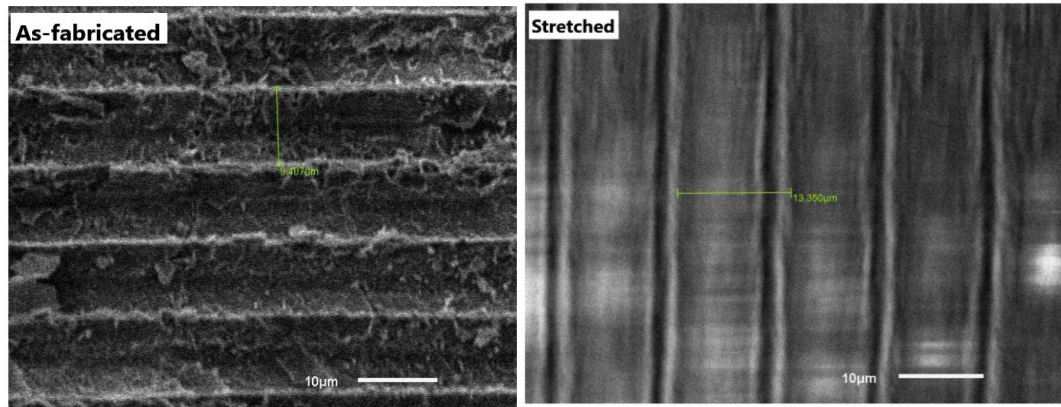
Figure 46: SEM images of the unstretched and stretched patterned graphene of the pitch size 9.4µm increased to 13.35µm, indicating a 42% graphene pitch strain.

4.5.3. Emissivity measurement

The emissivity was obtained by calculating the energy ratio between the patterned graphene and a blackbody furnace operating at the same temperature. Emissivity of patterned PDMS and patterned graphene on PDMS of the same 10 µm pitch size and PDMS thickness ~350 µm at 150°C was measured and calculated as shown in Figure 47 below. Patterned PDMS and patterned graphene on PDMS show the emissivity values of 0.5 and 0.6 respectively. Patterned graphene shows no prominent emissivity peak contribution from graphene at around 10 µm wavelength for the 10 µm pitch graphene pattern. The contribution of PDMS absorption is much stronger and dominates the spectrum.
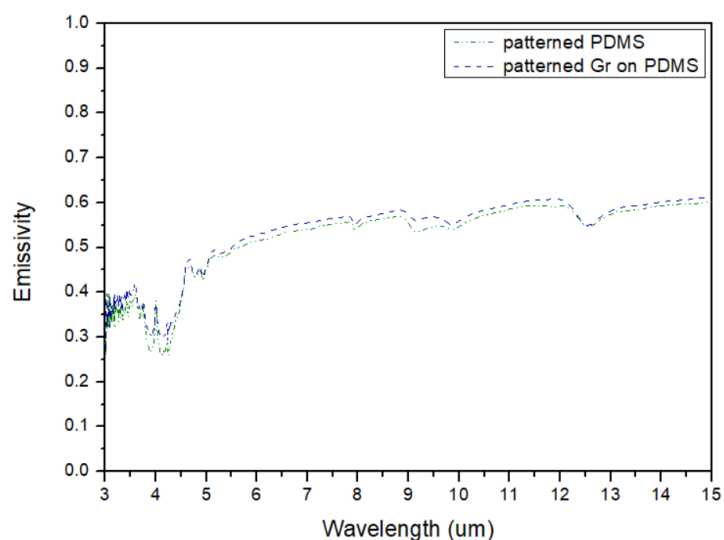
Figure 47: Emissivity of the patterned Graphene and PDMS of 10 µm pitch size measured at 150 °C showing insignificant intensity shift and same emissivity spectra.

Therefore, to see the emissivity effect of patterned graphene without PDMS, we fabricated the patterned graphene on nickel (see section 4.4.5). We measured the emissivity of nickel, flat graphene on nickel, and patterned graphene of 10 µm and 12 µm pitch on nickel at 150 °C. The thickness of the nickel film ~400 nm was constant for each sample. However, we couldn't observe prominent peak from patterned graphene on nickel. All samples show the similar emissivity spectra with a small intensity shift as shown in figure 48. Therefore, we increased the number of graphene layers to around 45 to observe the contribution of graphene in the emissivity spectra. From the emissivity measurements, we observed that graphene has no contribution in the tuning of emissivity in the mid-IR region. These results show that the graphene films on PDMS are heavily doped that the interband transitions for energies around IR wavelengths are suppressed by Pauli blocking.
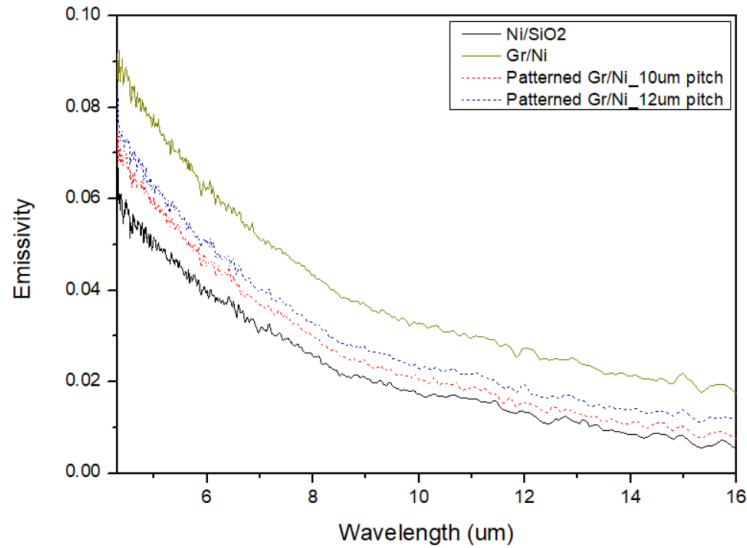
Figure 48: Emissivity of the nickel, graphene on nickel and patterned Gr/Ni of 10 µm and 12 µm pitch size measured at 150 °C. Patterned graphene depicts same emissivity profile as plain graphene.
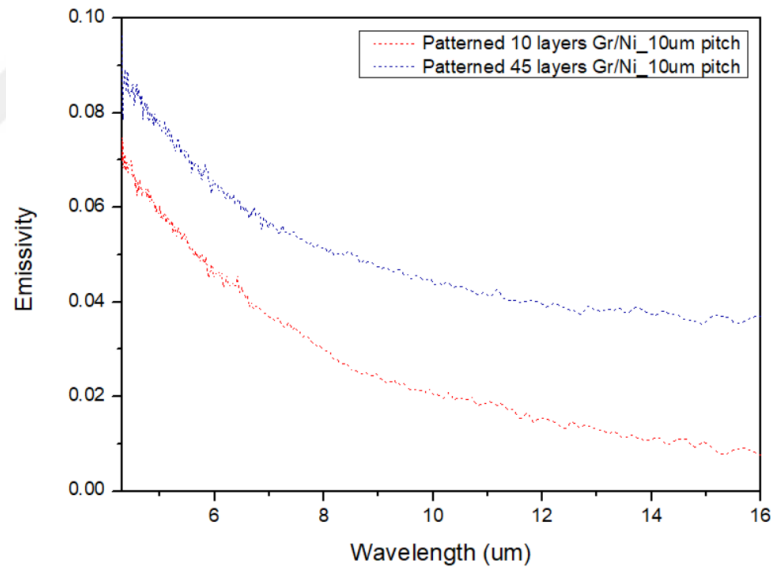
Figure 49: Comparison of the emissivity of different number of layers of patterned Gr of the same 10 µm periodicity measured at 150 °C. More number of graphene layers show same emissivity spectra as few graphene layers with an insignificant intensity shift.

The emissivity of the spontaneously corrugated Ni-PDMS film was also measured. The topography of the film is characterized by randomly distributed cracks, which widen by applied strain and lead to larger area of PDMS to be exposed. A sample with 100 nm thick Ni deposited on PDMS shows a prominent peak at around 10 µm wavelength which we

believe are due to the induced surface patterns of about 10 µm period. Mechanical strain up to 15% was applied to the sample which increase the intensity of the emissivity due to widening of the cracks that exposed the PDMS. Since PDMS has higher emissivity than Ni, there is a monotonous increase in intensity with respect to applied strain a shown in the figure 50. Moreover, we applied strain perpendicular to corrugation lines to increase the periodicity of the surface patterns. It was observed that sample with 100 nm Ni deposition on PDMS showed a prominent peak at around 10 µm wavelength which tends to shift to longer wavelengths with an increase in applied strain as shown in figure 51. Thus, the resulting emissivity from the Ni film and exposed PDMS can be reversibly modulated mechanically.
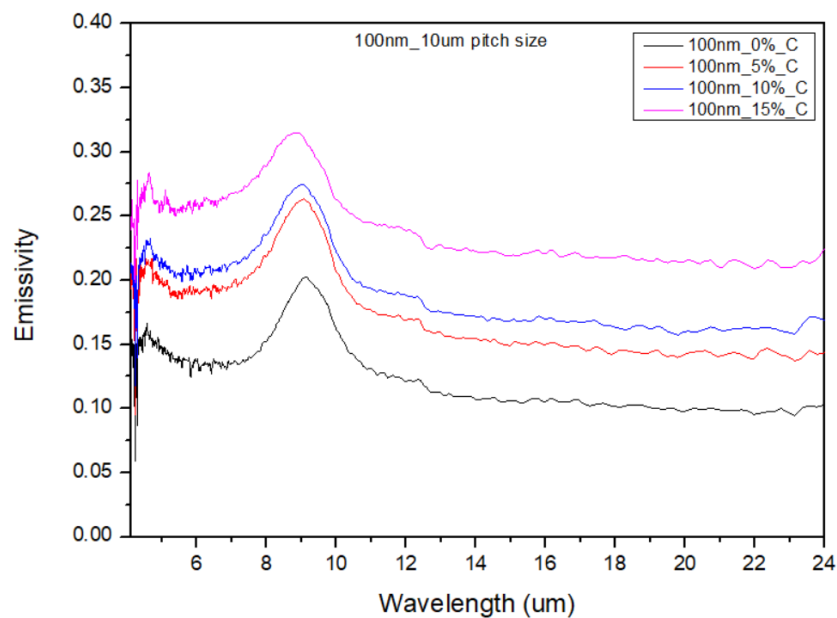
Figure 50: The emissivity spectra of Ni on PDMS of various strain applied perpendicular to the cracks to exposed beneath PDMS.
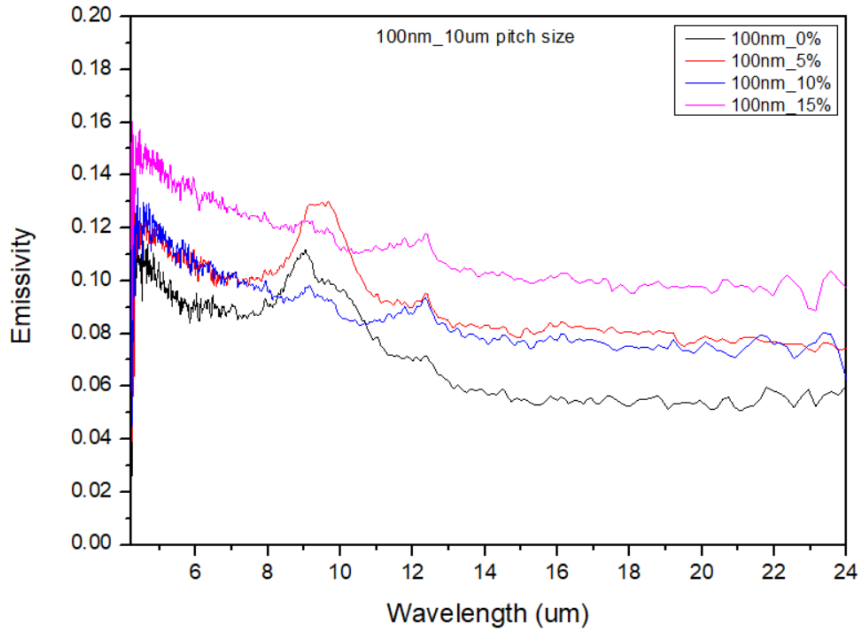
Figure 51: The emissivity spectra of the sample with 100 nm Ni at various strain to change the pitch size of the periodic surface patterns. Increasing the strain shifts the emissivity spectra to higher wavelength.

Similarly, the emissivity of the nickel, SiO_2 and pattern $Ni\text{-}SiO_2$ of 8, 10, 12, 14 µm periodicity was measured at 150 °C in the IR regions. The measured emissivity peaks around 9, 11, 13, and 15 were observed for 8, 10, 12, 14 µm periodic patterns of the same aspect ratio of Ni and SiO_2. Peak position shifted towards longer wavelengths with the increase in periodicity of the same aspect ratio patterns. However, changing the aspect ratio changes the intensity of the emissivity for the same periodicity. Increasing the ratio of SiO_2, shift the emissivity spectra upward and vice versa.
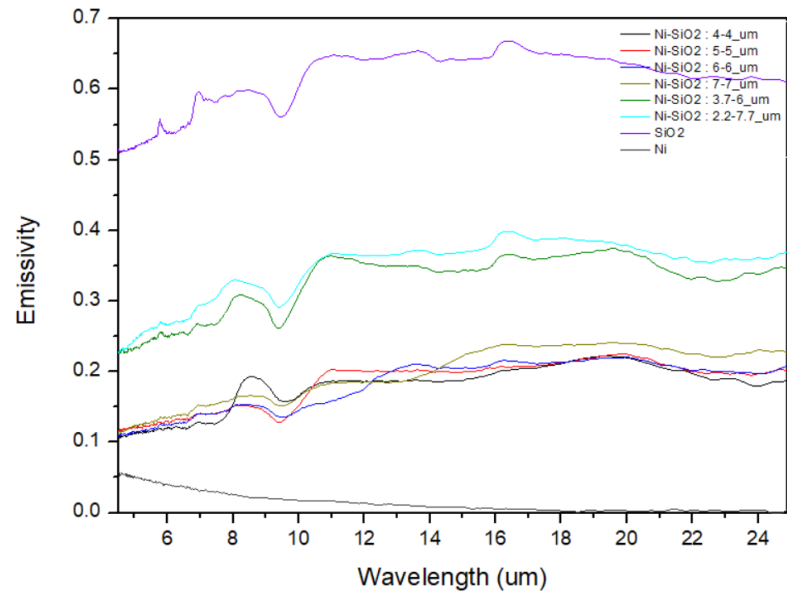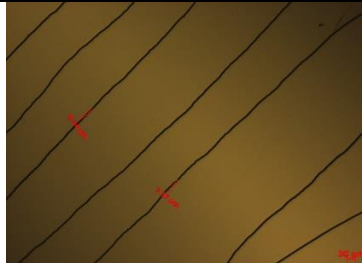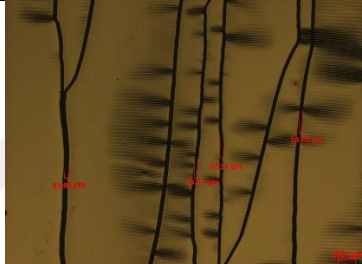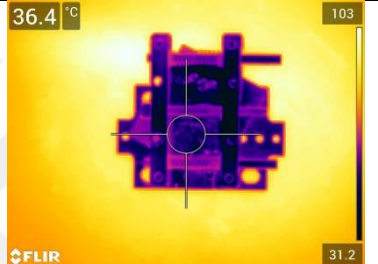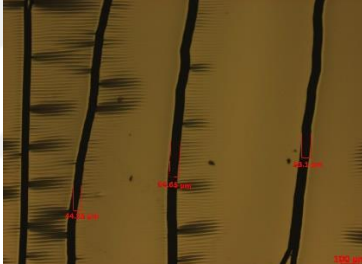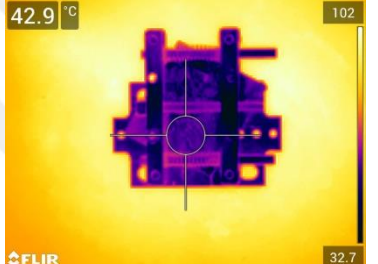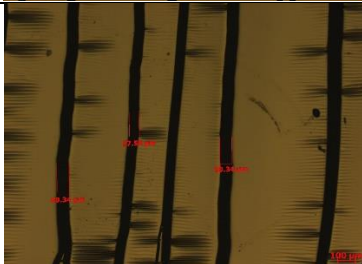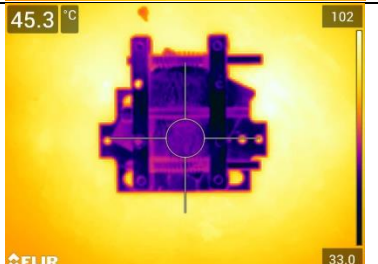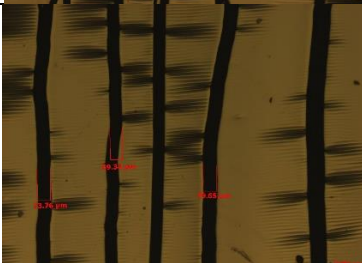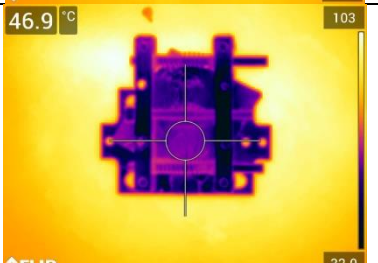
Figure 52: Emissivity of Ni, SiO$_2$ and patterned Ni-SiO$_2$ with 8, 10, 12 and 14 µm periods measured at 150 °C. Prominent periodicity peak is observed at the corresponding wavelength.

4.5.4. Thermal camera

A substrate is comprised of a thin layer of nickel film of low emissivity ($\varepsilon = 0.3$) atop of stretchable PDMS with a high emissivity ($\varepsilon = 0.6$). A stretching apparatus attached to a thermal contactor was attached to the substrate to maintain a same heating temperature with the hot plate. Different percentage strain, 0% to 20%, was applied and released to the substrate to generate a high and low width cracks on the nickel film composed of PDMS. The widening and narrowing of the cracks on the sample expose the PDMS by the simple mechanical strain. The substrates were uniformy heated to 100 °C by a hotplate to emit thermal radiation to be monitored by a thermal camera to observe any changes in temperature with the applied strain. 0% and 20% strain response of the substrate and their measured temperatures are shown in the table 4 below. The temperature changes from 35.9°C at 0% strain to 36.4°C, 42.9°C, 45.3°C, 46.9°C at 10%, 15%, and 20% strain respectively, demonstrating a temperature change of 11°C within a 20% strain.

Strain %	70 nm Ni on PDMS (°C)	200 nm Ni on PDMS
0	37.5	35.9
5	38.5	36.4
10	39.5	42.9
15	40.6	45.3
20	41.5	46.9
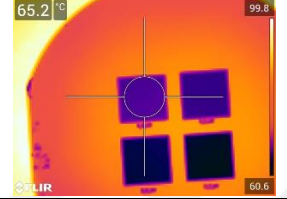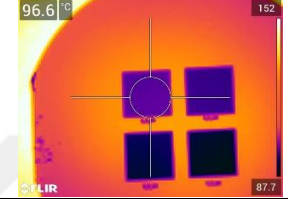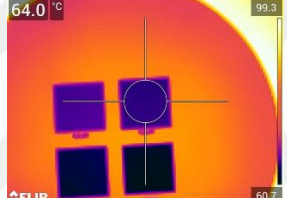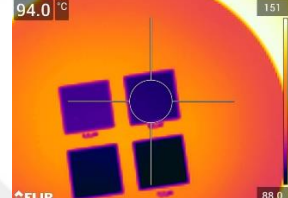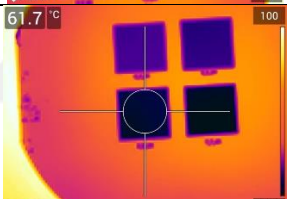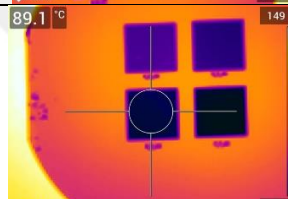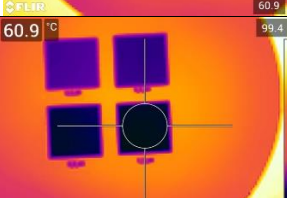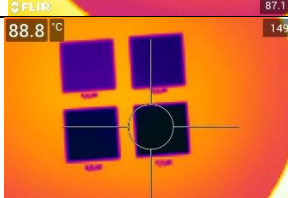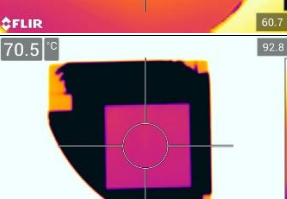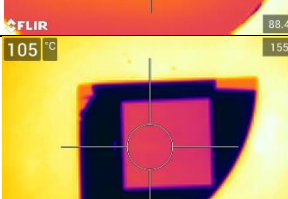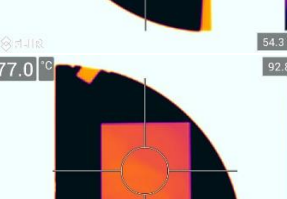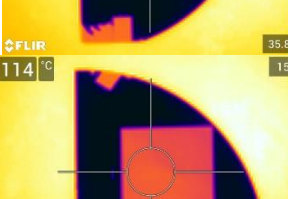
Table 4: Temperature readings from the surface of a spontaneously corrugated nickel surface at different strains. The sample has 200 nm Ni deposited on PDMS.

Strain (%)	Average crack width (µm)	Temp. reading on sample (°C)	OM Images	Thermal camera Images
0	8.40	35.9		
5	20.65	36.4		
10	50.67	42.9		
15	65.41	45.3		
20	74.25	46.9		

Similarly, patterned Ni-SiO$_2$ was also monitored by a thermal camera to observed the change in temperature of substrates with various periodicity and aspect ratio.

Temperatures were measured at two different hotplate temperatures set at 100 °C and 200 °C. Higher SiO_2/Ni ratio gives higher temperature reading since SiO_2 has higher emissivity than Ni.

Table 5: Temperature reading from the surfaces of periodically patterned Ni wires on SiO_2. hotplate set at 100 °C and 200 °C.

Ni-SiO_2 (µm)	Temperature reading on sample (Hotplate set at 100 °C)	Temperature reading on sample (Hotplate set at 150 °C)	Thermal camera Images (Hotplate set at 100 °C)	Thermal camera Images (Hotplate set at 150 °C)
4-4	65.2	96.6		
5-5	64.0	94.0		
6-6	61.7	89.1		
7-7	60.9	88.8		
3.7-6.0	70.5	105.0		
2.2-7.7	77.0	114.0		

5. CONCLUSIONS

The research for this thesis yielded the experimental results on the thermal radiation from modulated metal surfaces. The results show the capability to modify metal surfaces by mechanically induced strain on PDMS and metal surfaces by forming mold through electron beam lithography (EBL). The graphene was easily transferred to the stretchable PDMS leading to the large-scale flexible patterned graphene surface.

Firstly, we demonstrated the pseudo-periodic corrugation of the graphene surface on pre-stretched PDMS deposited with a soft skin layer by mechanical straining. The simplicity of CFx deposition on PDMS allows crack-free crumpled surface via a simple and cost-effective process. However, the pitch size of corrugated surface was inconsistent at different samples of the same parameters and graphene was unable to transfer on it.
Secondly, we demonstrated a transfer of monolayer graphene onto pre-strained patterned PDMS, treated with UV ozone, by mechanical straining. However, the transferred graphene is often broken and folded around the pre-patterned structures. Therefore, we synthesized multilayer graphene films using CVD on patterned nickel film and transferred them to a stretchable PDMS. The simplicity of UV ozone treatment allows the adhesion of graphene to PDMS via a simple process. The material integrity of graphene remains crack-free up to 100% strain. Predetermined corrugation via mold has an advantage over CFx induced generation of pseudo-periodic corrugation as it allows for controlled pitch size of graphene. Graphene shows low emissivity in the IR wavelengths due to doping caused by UVO treatment.

Additionally, low and high emissivity patterned materials, Ni-SiO$_2$ and Ni-PDMS, created enhancement or diminution in the emissivity at specific wavelengths related to the corrugation periodicity. We demonstrate a tunability of emissivity of these patterned

surfaces throughout the IR wavelength range. This image further explains our findings about the low emissivity of graphene on PDMS.

BIBLIOGRAPHY

1. Burch, D.E. and D.A. Gryvnak. *Laboratory Measurements Of The Infrared Absorption By H [sub] 2 [/sub] O And CO [sub] 2 [/sub] In Regions Of Weak Absorption*. in *Optical properties of the atmosphere*. 1978. SPIE.

2. Mahulikar, S., et al., *Numerical studies of infrared signature levels of complete aircraft.* The aeronautical journal, 2001. **105**(1046): p. 185-192.

3. Phan, L., et al., *Reconfigurable infrared camouflage coatings from a cephalopod protein.* Advanced Materials, 2013. **25**(39): p. 5621-5625.

4. Yu, C., et al., *Adaptive optoelectronic camouflage systems with designs inspired by cephalopod skins.* Proceedings of the National Academy of Sciences, 2014. **111**(36): p. 12998-13003.

5. Wang, G., et al., *Mechanical chameleon through dynamic real-time plasmonic tuning.* Acs Nano, 2016. **10**(2): p. 1788-1794.

6. Xiao, L., et al., *Fast adaptive thermal camouflage based on flexible VO2/graphene/CNT thin films.* Nano letters, 2015. **15**(12): p. 8365-8370.

7. Rubežienė, V., et al., *Evaluation of camouflage effectiveness of printed fabrics in visible and near infrared radiation spectral ranges.* Mater Sci-Medzg, 2008. **14**(4): p. 361-365.

8. Zhang, H. and J.C. Zhang, *Near-infrared green camouflage of cotton fabrics using vat dyes.* Journal of the Textile Institute, 2008. **99**(1): p. 83-88.

9. Salihoglu, O., et al., *Graphene-based adaptive thermal camouflage.* Nano letters, 2018. **18**(7): p. 4541-4548.

10. Chandrasekhar, P., et al., *Large, switchable electrochromism in the visible through far-infrared in conducting polymer devices.* Advanced Functional Materials, 2002. **12**(2): p. 95-103.

11. Krishna, A., et al., *Ultraviolet to mid-infrared emissivity control by mechanically reconfigurable graphene.* Nano letters, 2019. **19**(8): p. 5086-5092.

12. Inoue, T., et al., *Realization of dynamic thermal emission control.* Nature materials, 2014. **13**(10): p. 928-931.

13. Coppens, Z.J. and J.G. Valentine, *Spatial and temporal modulation of thermal emission.* Advanced Materials, 2017. **29**(39): p. 1701275.

14. Greffet, J.-J., et al., *Coherent emission of light by thermal sources.* Nature, 2002. **416**(6876): p. 61-64.

15. Diem, M., T. Koschny, and C.M. Soukoulis, *Wide-angle perfect absorber/thermal emitter in the terahertz regime.* Physical Review B, 2009. **79**(3): p. 033101.

16. Schuller, J.A., T. Taubner, and M.L. Brongersma, *Optical antenna thermal emitters.* Nature Photonics, 2009. **3**(11): p. 658-661.

17. Liu, X., et al., *Taming the blackbody with infrared metamaterials as selective thermal emitters.* Physical review letters, 2011. **107**(4): p. 045901.

18. Mason, J., S. Smith, and D. Wasserman, *Strong absorption and selective thermal emission from a midinfrared metamaterial.* Applied Physics Letters, 2011. **98**(24): p. 241105.

19. Costantini, D., et al., *Plasmonic metasurface for directional and frequency-selective thermal emission.* Physical Review Applied, 2015. **4**(1): p. 014023.

20. Liu, J., et al., *Quasi-coherent thermal emitter based on refractory plasmonic materials.* Optical Materials Express, 2015. **5**(12): p. 2721-2728.

21. Makhsiyan, M., et al., *Shaping the spatial and spectral emissivity at the diffraction limit.* Applied Physics Letters, 2015. **107**(25): p. 251103.

22. Roberts, A.S., et al., *Near-infrared tailored thermal emission from wafer-scale continuous-film resonators.* Optics express, 2015. **23**(19): p. A1111-A1119.

23. Zhou, M., et al., *Analog of superradiant emission in thermal emitters.* Physical Review B, 2015. **92**(2): p. 024302.

24. Huang, W.-L., et al., *Triple-wavelength infrared plasmonic thermal emitter using hybrid dielectric materials in periodic arrangement.* Applied Physics Letters, 2016. **109**(6): p. 063107.

25. Ilic, O., et al., *Tailoring high-temperature radiation and the resurrection of the incandescent source.* Nature nanotechnology, 2016. **11**(4): p. 320-324.

26. Liao, C.Y., et al., *Quasi-coherent thermal radiation with multiple resonant plasmonic cavities.* Applied Physics Letters, 2016. **109**(26): p. 261101.

27. Park, J.H., et al., *Observation of thermal beaming from tungsten and molybdenum bull's eyes.* ACS Photonics, 2016. **3**(3): p. 494-500.

28. Liu, B., et al., *Perfect thermal emission by nanoscale transmission line resonators.* Nano letters, 2017. **17**(2): p. 666-672.

29. Yang, Z.-Y., et al., *Narrowband wavelength selective thermal emitters by confined tamm plasmon polaritons.* Acs Photonics, 2017. **4**(9): p. 2212-2219.

30. Zhang, X., et al., *Controlling thermal emission of phonon by magnetic metasurfaces.* Scientific reports, 2017. **7**(1): p. 1-8.

31. Nagpal, P., et al., *Efficient low-temperature thermophotovoltaic emitters from metallic photonic crystals.* Nano letters, 2008. **8**(10): p. 3238-3243.

32. Chan, W.R., et al., *Toward high-energy-density, high-efficiency, and moderate-temperature chip-scale thermophotovoltaics.* Proceedings of the National Academy of Sciences, 2013. **110**(14): p. 5309-5314.

33. Lenert, A., et al., *A nanophotonic solar thermophotovoltaic device.* Nature nanotechnology, 2014. **9**(2): p. 126-130.

34. Rinnerbauer, V., et al., *Metallic photonic crystal absorber-emitter for efficient spectral control in high-temperature solar thermophotovoltaics.* Advanced Energy Materials, 2014. **4**(12): p. 1400334.

35. Asano, T., et al., *Near-infrared–to–visible highly selective thermal emitters based on an intrinsic semiconductor.* Science advances, 2016. **2**(12): p. e1600499.

36. Dyachenko, P.N., et al., *Controlling thermal emission with refractory epsilon-near-zero metamaterials via topological transitions.* Nature communications, 2016. **7**(1): p. 1-8.

37. Zhou, J., X. Chen, and L.J. Guo, *Efficient Thermal–Light Interconversions Based on Optical Topological Transition in the Metal-Dielectric Multilayered Metamaterials.* Advanced Materials, 2016. **28**(15): p. 3017-3023.

38. Miyazaki, H., et al., *Dual-band infrared metasurface thermal emitter for CO2 sensing.* Applied Physics Letters, 2014. **105**(12): p. 121107.

39. Lochbaum, A., et al., *On-chip narrowband thermal emitter for mid-IR optical gas sensing.* ACS photonics, 2017. **4**(6): p. 1371-1380.

40. Raman, A.P., et al., *Passive radiative cooling below ambient air temperature under direct sunlight.* Nature, 2014. **515**(7528): p. 540-544.

41. Zhu, L., A.P. Raman, and S. Fan, *Radiative cooling of solar absorbers using a visibly transparent photonic crystal thermal blackbody.* Proceedings of the national academy of sciences, 2015. **112**(40): p. 12282-12287.

42. Hsu, P.-C., et al., *Radiative human body cooling by nanoporous polyethylene textile.* Science, 2016. **353**(6303): p. 1019-1023.

43. Zhai, Y., et al., *Scalable-manufactured randomized glass-polymer hybrid metamaterial for daytime radiative cooling.* Science, 2017. **355**(6329): p. 1062-1066.

44. Li, Y., et al., *Temperature-dependent transformation thermotics: from switchable thermal cloaks to macroscopic thermal diodes.* Physical review letters, 2015. **115**(19): p. 195503.

45. Sun, Y., et al., *Flexible mid-infrared radiation modulator with multilayer graphene thin film by ionic liquid gating.* ACS applied materials & interfaces, 2019. **11**(14): p. 13538-13544.

46. Ergoktas, M.S., et al., *Multispectral graphene-based electro-optical surfaces with reversible tunability from visible to microwave wavelengths.* Nature photonics, 2021. **15**(7): p. 493-498.

47. Ding, P., et al., *Multilayer graphene-based radiation modulator for adaptive infrared camouflage with thermal management.* Journal of Physics D: Applied Physics, 2022.

48. Wang, Y., et al., *Super-elastic graphene ripples for flexible strain sensors.* ACS nano, 2011. **5**(5): p. 3645-3650.

49. Zang, J., et al., *Multifunctionality and control of the crumpling and unfolding of large-area graphene.* Nature materials, 2013. **12**(4): p. 321-325.

50. Leem, J., et al., *Mechanically self-assembled, three-dimensional graphene–gold hybrid nanostructures for advanced nanoplasmonic sensors.* Nano letters, 2015. **15**(11): p. 7684-7690.

51. Wang, M.C., et al., *Heterogeneous, three-dimensional texturing of graphene.* Nano letters, 2015. **15**(3): p. 1829-1835.

52. Lee, W.-K., et al., *Multiscale, hierarchical patterning of graphene by conformal wrinkling.* Nano letters, 2016. **16**(11): p. 7121-7127.

53. Rhee, D., W.K. Lee, and T.W. Odom, *Crack-Free, soft wrinkles enable switchable anisotropic wetting.* Angewandte Chemie, 2017. **129**(23): p. 6623-6627.

54. Deng, S., et al., *Graphene wrinkles enable spatially defined chemistry.* Nano letters, 2019. **19**(8): p. 5640-5646.

55. Rhee, D., et al., *Soft skin layers enable area-specific, multiscale graphene wrinkles with switchable orientations.* ACS nano, 2019. **14**(1): p. 166-174.

56. Yang, S., Y. Chen, and C. Jiang, *Strain engineering of two-dimensional materials: methods, properties, and applications.* InfoMat, 2021. **3**(4): p. 397-420.

57. Kang, P., et al., *Crumpled graphene photodetector with enhanced, strain-tunable, and wavelength-selective photoresponsivity.* Advanced Materials, 2016. **28**(23): p. 4639-4645.

58. Bao, Q. and K.P. Loh, *Graphene photonics, plasmonics, and broadband optoelectronic devices.* ACS nano, 2012. **6**(5): p. 3677-3694.

59. Bonaccorso, F., et al., *Graphene photonics and optoelectronics.* Nature photonics, 2010. **4**(9): p. 611-622.

60. Wallace, P.R., *The band theory of graphite.* Physical review, 1947. **71**(9): p. 622.

61. Charlier, J.-C., et al., *Electron and phonon properties of graphene: their relationship with carbon nanotubes*, in *Carbon nanotubes*. 2007, Springer. p. 673-709.

62. Novoselov, K.S. and A. Geim, *The rise of graphene.* Nat. Mater, 2007. **6**(3): p. 183-191.

63. Neto, A.C., et al., *The electronic properties of graphene.* Reviews of modern physics, 2009. **81**(1): p. 109.

64. Blake, P., et al., *Making graphene visible.* Applied physics letters, 2007. **91**(6): p. 063124.

65. Casiraghi, C., et al., *Rayleigh imaging of graphene and graphene layers.* Nano letters, 2007. **7**(9): p. 2711-2717.

66. Nair, R.R., et al., *Fine structure constant defines visual transparency of graphene.* science, 2008. **320**(5881): p. 1308-1308.

67. Hasan, T., et al., *Nanotube–polymer composites for ultrafast photonics.* Advanced materials, 2009. **21**(38-39): p. 3874-3899.

68. Sun, Z., et al., *Graphene mode-locked ultrafast laser.* ACS nano, 2010. **4**(2): p. 803-810.

69. Wu, S., *Nonlinear photoluminescence from graphene. Abstract number: BAPS. 2010.* MAR.

70. Hartschuh, A. *Excited state energies and decay dynamics in carbon nanotubes and graphene*. in *E-MRS Spring Meeting*. 2010.

71. Lui, C.H., et al., *Ultrafast photoluminescence from graphene.* Physical review letters, 2010. **105**(12): p. 127404.

72. Stöhr, R.J., et al., *Fluorescence of laser-created electron-hole plasma in graphene.* Physical Review B, 2010. **82**(12): p. 121408.

73. Sun, X., et al., *Nano-graphene oxide for cellular imaging and drug delivery.* Nano research, 2008. **1**(3): p. 203-212.

74. Gokus, T., et al., *Making graphene luminescent by oxygen plasma treatment.* ACS nano, 2009. **3**(12): p. 3963-3968.

75. Luo, Z., et al., *Photoluminescence and band gap modulation in graphene oxide.* Applied physics letters, 2009. **94**(11): p. 111909.

76. Eda, G., et al., *Blue photoluminescence from chemically derived graphene oxide.* Advanced materials, 2010. **22**(4): p. 505-509.

77. Zhang, G., et al., *Versatile polymer-free graphene transfer method and applications.* ACS applied materials & interfaces, 2016. **8**(12): p. 8008-8016.

78. Lin, W.-H., et al., *A direct and polymer-free method for transferring graphene grown by chemical vapor deposition to any substrate.* ACS nano, 2014. **8**(2): p. 1784-1791.

79. Sun, J., et al., *Electrochemical bubbling transfer of graphene using a polymer support with encapsulated air gap as permeation stopping layer.* Journal of Nanomaterials, 2016. **2016**.

80. Novoselov, K.S., et al., *A roadmap for graphene.* nature, 2012. **490**(7419): p. 192-200.

81. Zhan, Z., et al., *Pore-free bubbling delamination of chemical vapor deposited graphene from copper foils.* Journal of Materials Chemistry C, 2015. **3**(33): p. 8634-8641.

82. Li, X., et al., *Large-area synthesis of high-quality and uniform graphene films on copper foils.* science, 2009. **324**(5932): p. 1312-1314.

83. Liang, X., et al., *Toward clean and crackless transfer of graphene.* ACS nano, 2011. **5**(11): p. 9144-9153.

84. Jo, S.S., *Chemical vapor deposition (CVD) growth and optimal transfer processes for graphene*. 2018, Massachusetts Institute of Technology.

85. Chen, X., L. Zhang, and S. Chen, *Large area CVD growth of graphene.* Synthetic Metals, 2015. **210**: p. 95-108.

86. Lee, H.C., et al., *Review of the synthesis, transfer, characterization and growth mechanisms of single and multilayer graphene.* RSC advances, 2017. **7**(26): p. 15644-15693.

87. Lin, Y.-C., et al., *Graphene annealing: how clean can it be?* Nano letters, 2012. **12**(1): p. 414-419.

88. Lupina, G., et al., *Residual metallic contamination of transferred chemical vapor deposited graphene.* ACS nano, 2015. **9**(5): p. 4776-4785.

89. Roddaro, S., et al., *The optical visibility of graphene: interference colors of ultrathin graphite on SiO2.* Nano letters, 2007. **7**(9): p. 2707-2710.

90. Ferrari, A.C. and J. Robertson, *Raman spectroscopy of amorphous, nanostructured, diamond–like carbon, and nanodiamond.* Philosophical Transactions of the Royal Society of London. Series A: Mathematical, Physical and Engineering Sciences, 2004. **362**(1824): p. 2477-2512.

91. Ferrari, A.C., *Raman spectroscopy of graphene and graphite: Disorder, electron–phonon coupling, doping and nonadiabatic effects.* Solid state communications, 2007. **143**(1-2): p. 47-57.

92. Malard, L.M., et al., *Raman spectroscopy in graphene.* Physics reports, 2009. **473**(5-6): p. 51-87.

93. Li, X., et al., *Transfer of large-area graphene films for high-performance transparent conductive electrodes.* Nano letters, 2009. **9**(12): p. 4359-4363.

94. Zhu, S.-E., S. Yuan, and G. Janssen, *Optical transmittance of multilayer graphene.* Europhysics Letters, 2014. **108**(1): p. 17007.

95. Liu, M., J. Sun, and Q. Chen, *Influences of heating temperature on mechanical properties of polydimethylsiloxane.* Sensors and Actuators A: Physical, 2009. **151**(1): p. 42-45.

96. McDonald, J.C. and G.M. Whitesides, *Poly (dimethylsiloxane) as a material for fabricating microfluidic devices.* Accounts of chemical research, 2002. **35**(7): p. 491-499.

97. Cai, D., et al., *Optical absorption in transparent PDMS materials applied for multimode waveguides fabrication.* Optical materials, 2008. **30**(7): p. 1157-1161.

98. Stankova, N., et al., *Optical properties of polydimethylsiloxane (PDMS) during nanosecond laser processing.* Applied Surface Science, 2016. **374**: p. 96-103.

99. Noll, W., *Chemistry and technology of silicones.* 2012: Elsevier.

100. Berthier, E., E.W. Young, and D. Beebe, *Engineers are from PDMS-land, Biologists are from Polystyrenia.* Lab on a Chip, 2012. **12**(7): p. 1224-1237.

101. Johnston, I., et al., *Mechanical characterization of bulk Sylgard 184 for microfluidics and microengineering.* Journal of Micromechanics and Microengineering, 2014. **24**(3): p. 035017.

102. Chen, W., et al. *Surface micromachining of polydimethylsiloxane (pdms) for microfluidic biomedical applications.* in *16th international conference on miniaturized system for chemistry and life sciences october.* 2012.

103. Kamran, Y. and P.-L. Larsson, *Second-order effects at microindentation of elastic polymers using sharp indenters.* Materials & Design, 2011. **32**(6): p. 3645-3653.

104. Kim, T.K., J.K. Kim, and O.C. Jeong, *Measurement of nonlinear mechanical properties of PDMS elastomer.* Microelectronic Engineering, 2011. **88**(8): p. 1982-1985.

105. Lee, W., et al., *Effect of cyclic compression and curing agent concentration on the stabilization of mechanical properties of PDMS elastomer.* Materials & Design, 2016. **96**: p. 470-475.

106. Dogru, S., et al., *Poisson's ratio of PDMS thin films.* Polymer Testing, 2018. **69**: p. 375-384.

107. Khanafer, K., et al., *Effects of strain rate, mixing ratio, and stress–strain definition on the mechanical behavior of the polydimethylsiloxane (PDMS) material as related to its biological applications.* Biomedical microdevices, 2009. **11**: p. 503-508.

108. Liu, M. and Q. Chen, *Characterization study of bonded and unbonded polydimethylsiloxane aimed for bio-micro-electromechanical systems-related applications.* Journal of Micro/Nanolithography, MEMS, and MOEMS, 2007. **6**(2): p. 023008.

109. Chen, K., A. Wo, and Y. Chen. *Transmission spectrum of PDMS in 4–7 μm mid-IR range for characterization of protein structure.* in *Nsti-Nanotech.* 2006.

110. Bowden, N., et al., *Spontaneous formation of ordered structures in thin films of metals supported on an elastomeric polymer.* nature, 1998. **393**(6681): p. 146-149.

111. Genzer, J. and J. Groenewold, *Soft matter with hard skin: From skin wrinkles to templating and material characterization.* Soft Matter, 2006. **2**(4): p. 310-323.

112. Tokudome, Y., et al., *Hierarchical Nested Wrinkles on Silica− Polymer Hybrid Films: Stimuli-Responsive Micro Periodic Surface Architectures.* Scientific reports, 2012. **2**(1): p. 1-6.

113. Yin, J., et al., *Surface wrinkling on polydimethylsiloxane microspheres via wet surface chemical oxidation.* Scientific reports, 2014. **4**(1): p. 1-8.

114. Hu, W., et al., *Sub-10 nm electron beam lithography using cold development of poly (methylmethacrylate).* Journal of Vacuum Science & Technology B: Microelectronics and Nanometer Structures Processing, Measurement, and Phenomena, 2004. **22**(4): p. 1711-1716.

115. Taniguchi, J., et al., *Rapid and three-dimensional nanoimprint template fabrication technology using focused ion beam lithography.* Microelectronic Engineering, 2006. **83**(4-9): p. 940-943.

116.   Ishii, Y. and J. Taniguchi, *Fabrication of three-dimensional nanoimprint mold using inorganic resist in low accelerating voltage electron beam lithography.* Microelectronic engineering, 2007. **84**(5-8): p. 912-915.

117.   Chen, Y., D. Macintyre, and S. Thoms, *Electron beam lithography process for T-and Γ-shaped gate fabrication using chemically amplified DUV resists and PMMA.* Journal of Vacuum Science & Technology B: Microelectronics and Nanometer Structures Processing, Measurement, and Phenomena, 1999. **17**(6): p. 2507-2511.

118.   Chen, Y., *Nanofabrication by electron beam lithography and its applications: A review.* Microelectronic Engineering, 2015. **135**: p. 57-72.

119.   Chou, S.Y., P.R. Krauss, and P.J. Renstrom, *Nanoimprint lithography.* Journal of Vacuum Science & Technology B: Microelectronics and Nanometer Structures Processing, Measurement, and Phenomena, 1996. **14**(6): p. 4129-4133.

120.   Ye, D., et al., *UV nanoimprint lithography of sub-100 nm nanostructures using a novel UV curable epoxy siloxane polymer.* Microelectronic engineering, 2010. **87**(11): p. 2411-2415.

121.   Hauser, H., et al., *Nanoimprint lithography for honeycomb texturing of multicrystalline silicon.* Energy Procedia, 2011. **8**: p. 648-653.

122.   Lim, H., et al., *Roller nanoimprint lithography for flexible electronic devices of a sub-micron scale.* Microelectronic engineering, 2011. **88**(8): p. 2017-2020.

123.   Unno, N. and J. Taniguchi, *Fabrication of the metal nano pattern on plastic substrate using roll nanoimprint.* Microelectronic engineering, 2011. **88**(8): p. 2149-2153.

124.   Liu, F., P. Ming, and J. Li, *Ab initio calculation of ideal strength and phonon instability of graphene under tension.* Physical Review B, 2007. **76**(6): p. 064120.

125.   Lee, C., et al., *Measurement of the elastic properties and intrinsic strength of monolayer graphene.* science, 2008. **321**(5887): p. 385-388.

126.   Kim, K.S., et al., *Large-scale pattern growth of graphene films for stretchable transparent electrodes.* nature, 2009. **457**(7230): p. 706-710.

127.   Bae, S., et al., *Roll-to-roll production of 30-inch graphene films for transparent electrodes.* Nature nanotechnology, 2010. **5**(8): p. 574-578.

128.   Bhaviripudi, S., et al., *Role of kinetic factors in chemical vapor deposition synthesis of uniform large area graphene using copper catalyst.* Nano letters, 2010. **10**(10): p. 4128-4133.

129.   Wu, Y., et al., *Synthesis of large-area graphene on molybdenum foils by chemical vapor deposition.* Carbon, 2012. **50**(14): p. 5226-5231.

130.   Gao, L., et al., *Repeated growth and bubbling transfer of graphene with millimetre-size single-crystal grains using platinum.* Nature communications, 2012. **3**(1): p. 1-7.

131.   Kim, J., et al., *Layer-resolved graphene transfer via engineered strain layers.* Science, 2013. **342**(6160): p. 833-836.

132.   Martins, L.G., et al., *Direct transfer of graphene onto flexible substrates.* Proceedings of the National Academy of Sciences, 2013. **110**(44): p. 17762-17767.

133.   Gao, L., et al., *Face-to-face transfer of wafer-scale graphene films.* Nature, 2014. **505**(7482): p. 190-194.

134.   Nguyen, N.N., et al., *Atomically thin epitaxial template for organic crystal growth using graphene with controlled surface wettability.* Nano Letters, 2015. **15**(4): p. 2474-2484.

135.   Yang, J., et al., *MoS2 liquid cell electron microscopy through clean and fast polymer-free MoS2 transfer.* Nano letters, 2019. **19**(3): p. 1788-1795.

136.   Lanza, M., et al., *Graphene-coated atomic force microscope tips for reliable nanoscale electrical characterization.* Advanced Materials (Deerfield Beach, Fla.), 2012. **25**(10): p. 1440-1444.

137.   Shim, W., et al., *Multifunctional cantilever-free scanning probe arrays coated with multilayer graphene.* Proceedings of the National Academy of Sciences, 2012. **109**(45): p. 18312-18317.

138.   Winters, S., et al., *Production of 3D-shaped graphene via transfer printing.* physica status solidi (b), 2012. **249**(12): p. 2515-2518.

139. Reserbat-Plantey, A., et al., *Strain superlattices and macroscale suspension of graphene induced by corrugated substrates.* Nano letters, 2014. **14**(9): p. 5044-5051.

140. Choi, J., et al., *Three-dimensional integration of graphene via swelling, shrinking, and adaptation.* Nano letters, 2015. **15**(7): p. 4525-4531.

141. Wei, Z., D.E. Barlow, and P.E. Sheehan, *The assembly of single-layer graphene oxide and graphene using molecular templates.* Nano letters, 2008. **8**(10): p. 3141-3145.

142. Liu, L., et al., *Graphene oxidation: thickness-dependent etching and strong chemical doping.* Nano letters, 2008. **8**(7): p. 1965-1970.

143. Felten, A., et al., *Controlled modification of mono-and bilayer graphene in O2, H2 and CF4 plasmas.* Nanotechnology, 2013. **24**(35): p. 355705.

144. Felten, A., et al., *Single-and Double-Sided Chemical Functionalization of Bilayer Graphene.* Small, 2013. **9**(4): p. 631-639.

145. Leconte, N., et al., *Damaging graphene with ozone treatment: a chemically tunable metal− insulator transition.* ACS nano, 2010. **4**(7): p. 4033-4038.

146. Luo, Z., et al., *Controlled doping of graphene using ultraviolet irradiation.* Applied Physics Letters, 2012. **100**(25): p. 253108.

147. Zhang, E., et al., *Ozone-exposure and annealing effects on graphene-on-SiO2 transistors.* Applied physics letters, 2012. **101**(12): p. 121601.

148. Imamura, G. and K. Saiki, *Modification of graphene/SiO2 interface by UV-irradiation: effect on electrical characteristics.* ACS applied materials & interfaces, 2015. **7**(4): p. 2439-2443.

149. Shenoy, G.J., et al., *Substrate dependent photochemical oxidation of monolayer graphene.* RSC advances, 2016. **6**(10): p. 8489-8494.

150. Sun, H., et al., *High quality graphene films with a clean surface prepared by an UV/ozone assisted transfer process.* Journal of Materials Chemistry C, 2017. **5**(8): p. 1880-1884.

151. Ryu, G.H., et al., *Effects of dry oxidation treatments on monolayer graphene.* 2D Materials, 2017. **4**(2): p. 024011.

152. Meyer, J.C., et al., *The structure of suspended graphene sheets.* Nature, 2007. **446**(7131): p. 60-63.

153. Fan, X., R. Nouchi, and K. Tanigaki, *Effect of charge puddles and ripples on the chemical reactivity of single layer graphene supported by SiO2/Si substrate.* The Journal of Physical Chemistry C, 2011. **115**(26): p. 12960-12964.

154. Emelianov, A., et al., *The effect of ultraviolet light on structural properties of exfoliated and CVD graphene.* Applied Physics Letters, 2016. **109**(17): p. 173101.